SANDIA REPORT
SAND2012-9186
Unlimited Release
Printed November 2012

Advanced Inactive Materials for Improved Lithium-Ion Battery Safety

Christopher J. Orendorff, Ganesan Nagasubramanian, Timothy N. Lambert, Kyle R. Fenton, Christopher A. Apblett, Christopher R. Shaddix, Manfred Geier, and E. Peter Roth

Prepared by
Sandia National Laboratories
Albuquerque, New Mexico 87185 and Livermore, California 94550

Sandia National Laboratories is a multi-program laboratory managed and operated by Sandia Corporation, a wholly owned subsidiary of Lockheed Martin Corporation, for the U.S. Department of Energy's National Nuclear Security Administration under contract DE-AC04-94AL85000.

Issued by Sandia National Laboratories, operated for the United States Department of Energy by Sandia Corporation.

Available to DOE and DOE contractors from
U.S. Department of Energy
Office of Scientific and Technical Information
P.O. Box 62
Oak Ridge, TN 37831

Telephone: (865) 576-8401
Facsimile: (865) 576-5728
E-Mail: reports@adonis.osti.gov
Online ordering: http://www.osti.gov/bridge

Available to the public from
U.S. Department of Commerce
National Technical Information Service
5285 Port Royal Rd.
Springfield, VA 22161

Telephone: (800) 553-6847
Facsimile: (703) 605-6900
E-Mail: orders@ntis.fedworld.gov
Online order: http://www.ntis.gov/help/ordermethods.asp?loc=7-4-0#online

SAND2012-9186
Unlimited Release
Printed November 2012

Advanced Inactive Materials for Improved Lithium-Ion Battery Safety

Christopher J. Orendorff[1], Ganesan Nagasubramanian[1], Timothy N. Lambert[2], Kyle R. Fenton[1], Christopher A. Apblett[1], Christopher R. Shaddix[3], Manfred Geier[3], and E. Peter Roth[1]

[1]Advanced Power Sources Research and Development
[2]Materials, Devices, and Energy Technology
[3]Hydrogen and Combustion Technology

Sandia National Laboratories
P.O. Box 5800
Albuquerque, New Mexico 87185-MS0614

Abstract

This report describes advances in lithium-ion battery safety by use of alternative electrolytes and separators. Electrolytes based on hydrofluoro ether solvents and sulfonimide salts were characterized to determine electrochemical performance, thermal stability, and decomposition products. Flammability of these electrolytes was also tested under known cell failure mode conditions. Separators based on high melting temperature polymers and ceramics were developed by fiber spinning, casting, and vapor deposition techniques. Resulting high melt integrity separators show good electrochemical performance and improved thermal stability compared to commercial polyolefin separator materials.

ACKNOWLEDGMENTS

This work was supported by the Sandia Laboratory Directed Research and Development (LDRD) program. Authors gratefully acknowledge technical contributions to this work by Lorie Davis, Jill Langendorf, David Johnson, Denise Bencoe, Carlos Chavez, Marlene Bencomo, Richard Grant and Bonnie McKenzie.

CONTENTS

FIGURES

TABLES

NOMENCLATURE

EV	electric vehicle
PHEV	plug-in hybrid electric vehicle
ARC	accelerating rate calorimetry or accelerating rate calorimeter
DSC	differential scanning calorimetry or differential scanning calorimeter
EC	ethylene carbonate
EMC	ethylmethyl carbonate
DEC	diethyl carbonate
PC	propylene carbonate
HFE	hydrofluoro ether
TPTP	2-trifluoro-2-fluoro-3-difluoropropoxy-3-difluoro-4-fluoro-5-trifluoropentane
TMMP	2-trifluoromethyl-3-methoxyperfluoropentane
FR	fire retardant or flame retardant
IL	ionic liquid
ASTM	American Society for Testing and Materials
UL	Underwriters Laboratories
IEC	International Electrotechnical Commission
SET	self-extinguishing time
LOI	limited oxygen index
PBT	poly(butylene) terephthalate
NMC	lithium nickel manganese cobalt oxide
NCA	lithium nickel cobalt aluminum oxide
PVDF	poly(vinylidene fluoride)
SEM	scanning electron microscopy or scanning electron micrograph
DOE	Department of Energy
SNL	Sandia National Laboratories

1. INTRODUCTION

As the use of lithium-ion cells for high power applications becomes increasingly widespread, safety and reliability of these cells and battery packs is of paramount importance. While most of the targets for lithium-ion in utility storage or transportation are focused on cost, cycle life, and performance, safety will be increasingly important as these batteries continue to grow in size to meet demand. Investment has been made to improve the safety and reliability anode and cathode materials, however, the most common field failures of electrolyte and separator represent notable hazards and have largely been overlooked until recently. In fact, recent high profile safety incidents in the emerging electric vehicle (EV) markets were directly related to electrolyte flammability [1]. The objective of this work is to better understand degradation of battery electrolytes and separators and to mitigate the hazards associated with these processes through materials processing development, full-cell performance evaluation and abuse testing.

1.1. Lithium-Ion Battery Electrolytes

Lithium batteries use organic electrolytes because of the wide operating voltage (up to 4.5 V vs. Li/Li^+) relative to other electrochemical couples. For lithium ion rechargeable batteries, these electrolytes are almost universally based on lithium hexafluorophosphate ($LiPF_6$) salts with combinations of linear and cyclic alkyl carbonates. These electrolytes enable the use of lithium as the negative electrode active component and results in the high power and energy densities characteristic of the Li-ion chemistries. However, these organic electrolyte solvents have high volatility and flammability that pose a serious safety issue for their use in the consumer and transportation markets. For example, gas generation in Li-ion cells under abuse conditions has an effect on safety because gas production, if generated at sufficient pressure will vent flammable solvent vapor into the surrounding environment. The resulting fuel-air mixture can be quite explosive and only requires an ignition source to ignite the vapors. $LiPF_6$ is known to react with carbonate solvents at elevated temperature and in the presence of moisture to generate large gas volumes of decomposition products [2-4].

Electrolytes for lithium-ion batteries are developed to meet performance criteria such as conductivity, temperature range (high and low) and voltage range stability. In fact a great deal of work has focused on correlating the relationship between performance criteria to selection of solvent species, solvent ratios, electrolyte salts and additives [5-6]. The choice of electrolyte can also have a significant impact on the safety, thermal stability and abuse tolerance of the cell. For example, some materials that have superior performance properties, such as $LiAsF_6$, cannot be used because of high toxicity [7]. Some solvent species, such as propylene carbonate (PC), are limited in concentration because they cause disruption of the anode graphite grains [8]. However, there are few studies that correlate the influence of electrolyte on the cell response during an abuse event. This work aims to design electrolytes for both electrochemical performance and safety and to develop testing methods for electrolyte flammability under cell venting conditions (known failure modes for lithium-ion cells).

1.2. Lithium-Ion Battery Separators

Another critically important cell component to ensure cell safety is the separator, a thin porous membrane that physically separates the anode and cathode. The primary function of the separator is to prevent physical contact between the anode and cathode, while facilitating ion transport in the cell. The challenge with designing safe battery separators is that trade-off between mechanical robustness and porosity/transport properties. Separator design is further complicated by additional constraints including tolerance to abuse conditions, stable at > 4V, chemically inert to other cell materials, and low cost to meet the performance and cost targets.

Most commercially available non-aqueous lithium-ion separators designed for small batteries (<3 Ah) are single layer or multilayer polymer sheets typically made of polyolefins. Most commonly, these are polyethylene (PE) or polypropylene (PP) which have transition temperatures of 135 and 165 °C, respectively, but is somewhat dependent on molecular weight. Polyethylene terephthalate (PET) and poly vinylidene fluoride (PVdF) have also been used in commercial separators, but are far less commonplace than the polyolefin films. These separators are highly porous, typically >40% porosity, approximately 25 μm thick, have low ionic resistivity (1.5-2.5 Ω-cm2) and have bulk puncture strengths >300 g/mil [9-11]. Ideally separators would be much thinner than 25 μm from a performance perspective and there are examples of separators that are as thin as 12-20 μm, however a great deal of mechanical strength is lost for the very thin membranes. Separators are typically manufactured by either an extrusion processes (wet or dry) followed by a mechanical stretching process to induce porosity or from wet-laid fibers to make non-woven mats [9-11].

There are also examples of separators composed of polymer/ceramic composites [12-18]. However, most of these examples are research scale and are faced with market challenges for lithium-ion batteries because of cost barriers. One of the first examples of a commercialized composite separator was Separion® introduced by Degussa, which is a trilayer membrane with two layers of ceramic (SiO_2/Al_2O_3) supported on either side of a porous polyethylene terephthalate (PET) film [19,20]. A table of common commercially available separators and their properties is shown in Table 1.

Table 1. Commercial separator properties found on data sheets for each product.

	Entek	Exxon	Degussa	Celgard
Product	Teklon	Tonen	Separion	2325
Thickness (μm)	25	25	25	25
Single/multilayer	Single layer	Single layer	Trilayer	Trilayer
Composition	PE	PE	Ceramic-PET-Ceramic	PP-PE-PP
Process	Wet extruded	Wet extruded	Wet-laid mat	Dry extruded
Porosity (%)	38	36	>40	41
Melt temperature (°C)	135	135	220	134/166

Many of the multilayer all polymer separators are designed with a shutdown feature, notably designed for small batteries and electronics applications. This shutdown feature works by one component of the separator melting at a lower temperature than the other, filling in the pores and stopping current flow in the cell. In general, polyolefin shutdown separators have been shown to be effective in small cells (<3 Ah) for lower voltage (<12 V) applications.[9] However, for higher capacity cells in larger batteries for transportation or grid storage application, separators designed for consumer electronics cells may not be applicable and may cause unintended failure modes in cells due to the phase transitions of these polyolefins [21]. Previous work on composite materials show that separators composed of more thermally stable materials have a direct impact on abuse tolerance and cell safety [21]. The work in this report highlights the weaknesses of some separator designs and improvements that can be made using thermally stable materials and alternative processing techniques.

2. NONFLAMMABLE ELECTROLYTES

2.1. Strategies for Nonflammable Electrolytes

Flammability of vented electrolyte solvent vapor continues to be a significant unresolved safety issue for lithium-ion batteries. Venting electrolyte is a complex mixture of solvent in the liquid and vapor phase, decomposition gases, and air. Flammability of this dynamic mixture is a function of solvent vapor pressure, heat of vaporization, heat of combustion, and surrounding environmental conditions of temperature and pressure [22-23]. The flammability of this mixture depends on the ratio of fuel and air which can vary significantly around the venting cell, especially with turbulent mixing that can occur from a rapidly venting cell. Rapid cell venting can displace air immediately around the cell which leads to an oxygen starved mixture that will not ignite. A highly diluted mixture of fuel to air may occur sufficiently far away from the venting cell and this lean solvent-air mixture also will not ignite. However, there will be regions around the cell where the fuel-air mixture is in the flammability range and will combust if an ignition source is present.

There are two general approaches to mitigating electrolyte flammability: (1) the use of flame retardant (FR) additives in the electrolyte formulation, or (2) the use of inherently nonflammable electrolyte solvents or co-solvents. Work on FR additives is mentioned briefly in this report, but this project is focused on the inherently nonflammable electrolyte co-solvent approach.

2.2. Flame retardant additives

One approach is to use fire retardants (FRs) in the electrolyte as an additive to suppress fire and thus improve thermal stability. Most of these additives have a history of use as FRs in plastics and the investigators chose to study them because of the assumption that the mechanism for flame suppression would be similar in liquid electrolytes for batteries. Several different materials have been investigated as FR additives. Broadly, these additives can be grouped into two types—those containing phosphorous or fluorine.

Table 2. List of fire retardants (FRs) studied for use in Li-ion batteries.

Name of FR	Reference
Phosphate/Phosphonate	
Triphenylphosphate (TPP)	[24]
vinyl ethylene carbonate (VEC) + biphenyl (BP) + TPP	[25]
Dimethyl methylphosphonate (DMMP)	[26] [27]
Polyphosphonate	[28]
Triphenyl phosphate (TPP), tris(trifluoroethyl)phosphate (TFP)	[29]
Phosphorus-containing esters	[30]
Methoxyethoxyethoxyphosphazenes	[31]
Bis(N,N-diethyl)methoxyethoxymethylphosphonamidate	[32]
Triphenyl Phosphate (TPP) and Trinutyl Phosphate (TBP)	[33]
Trimethyl Phosphate (TMP) and Triethyl Phosphate (TEP)	[34]
Ethylene Ethyl Phosphate(EEP) + TMP	[35]
Diphenyloctyl phosphate(DPLP)	[36]
Cyclic phosphate	[37]
Phosphites	
Tris(2,2,2-Trifluoroethyl) Phosphite (TTFP)	[38, 39]
Triethyl and Tributyl Phosphite	[40]
Trimethyl phosphite (TMP)	[41]
Phosphazenes	
Phoslyte	[42]
Ethyleneoxy Phosphazenes	[31, 43]
Phosphazene-based flame retardants	[44]
Hexamethoxycyclotriphosphazene	[45, 46]
Miscellaneous compounds	
Hexamethylphosphoramide (HMPA)	[47]
Dimethyl Methylphosphonate (DMMP)	[48]

In the vapor phase, the traditionally accepted mechanism is that the FR decomposes producing phosphorous or halogen radicals that act as scavengers and react with hydrogen radicals, thereby terminating the free radical reaction [49]. Despite wide availability of FR materials, two primary classes of materials have been investigated extensively for use in Li-ion batteries, which are phosphorus and fluorine containing materials. The phosphorous containing materials primarily rely on the free radical scavenging mechanism, but on rare occasion inhibit reaction through char formation on the reactive surface. The fluorinate materials have been studied as cosolvents in electrolytes and as FR additives. Since the C-F bond (105.4 kcal mol^{-1}) is stronger than the C-H bond (98.8 kcal mol^{-1}) [50], more heat energy is required to cleave the bond, the fluorinated solvents are thermally more stable than the non-fluorinated analogs. When used as additive the FR decomposes generating F· radicals which combine with the H· (remember H· is one of the radicals that sustains combustion and by annihilating the H· there could be minimal or no fire in the electrolyte) and quenches the free radical reaction and stops the flame propagation.

Numerous flame retardant additives have been tested in most of the standard Li-ion electrolytes with mixed results as indicated in Table 2 [24-48]. Often, the amount of additive required to achieve non-flammability significantly reduces cell performance. Furthermore, some of the additives are not stable with the active electrode materials, especially against reduction at the anode. Use of flame retardant additives then requires additional additives to stabilize the anode. The long-term effect of these additives on the cell lifetime and performance is not known. One of the major difficulties in evaluating the effectiveness of the flame retardant is a meaningful test that simulates the environment of a venting Li-ion cell. Most tests are based on open flame or burning wick type configurations. These tests are useful for evaluating the relative performance of different additives but do not adequately recreate the conditions of a vented cell that produces solvent vapor at elevated temperature and pressure. Flammability needs to be determined with full cells under controlled thermal conditions with multiple ignition sources to test for different fuel/air ratios [49]. Several claimed non-flammable electrolytes using fire retardant additives have been shown to result in burning gas mixtures from real-world venting cells [29].

2.3. Inherently nonflammable electrolytes

Another approach to addressing electrolyte flammability is the use of inherently nonflammable electrolyte solvents. Table 3 lists the high Fp co-solvents that have been reported in the literature for use in lithium-ion batteries. As described above, one of the challenges with the additive approach is that the FRs are present in such small quantities that the flammability/ignition response of the total electrolyte solvent is dominated by the low flash point (F_p) components (defined as “the lowest temperature at which it can vaporize to form an ignitable mixture in air”) [51]. In designing nonflammable electrolytes, one approach is to focus on making solvent choices from materials that have higher flash points (or no flash point) than linear carbonates. However, this is a significant challenge given the complexities of a lithium-ion cell including wide operating voltage, stability at the lithium potential, aprotic, a broad working temperature range, chemically inert, good separator wettability, and must promote good lithium salt dissolution.

Table 3. List of co-solvents or alternative solvents studied for use in Li-ion batteries.

Name of Solvent/Additive	Reference
Fluorinated Phosphate/Ethers	
Tris(Trifluoroethyl)Phosphate (TFP), Bis(trifluoroethyl)Methyl Phosphate (BMP) and Trifluoroethyl Phosphate (TDP)	[52, 53]
Methyl Nonafluorobutyl Ether (EFE)	[54, 55]
Perfluoro-Ether	[56]
Hydrofluoro Ether (HFE)	[57, 58]
Ionic Liquids	
N-butyl-N-methylpyrrolidinium bis(fluorosulfonyl)imide (PYR14FSI)	[59, 60]
N-butyl-N-methylpyrrolidinium bis(trifluoromethansulfonyl)imide, PYR14TFSI	[61]
1-ethyl-3- Methylimidazolium tetrafluoroborate (EMIBF4)	[62]
Tri-(4-methoxythphenyl) phosphate (TMTP)	[63]

Table 4 compares the F_P for several solvents, where a lower F_p is easier to ignite than the higher F_p. For example: dimethyl carbonate is a commonly used combustible solvent in lithium-ion cells and has an F_P of 18 ºC, whereas canola oil is non-combustible and has a F_P of 327 ºC. For comparisons to the transportation industry, gasoline has an F_p of -42 ºC.

Table 4. Flash Point* for some of the common organic solvents.

Chemical	Flash Point (ºC)
Acetone	-17
Ethanol	17
Gasoline	-42
DEC	33
DMC	18
EMC	23
EC	145
PC	132
HFEs (TMMP, TPTP)	No flash point
IL (1-ethyl-3-methyl imadazolium TFSI)	283
Canola oil	327

*= As per OSHA (Occupational Safety & Health Administration) classification any liquid with a flash point below 38.7 ºC is flammable.

Ionic liquids (ILs) are one class of compounds that have high flash points and have been studied as alternative solvents for lithium-ion electrolytes [64]. The data published in the literature show that polyphosphazene polymers and ionic liquids used as electrolytes are nonflammable. However, the high flash point is generally accompanied by increased viscosity, thus limiting low temperature operation and degrading cell performance at sub-ambient temperatures. These materials may not be suitable for wide temperature operation and may also have other problems such as poor wetting of the electrodes and separator materials, excluding them from use in cells despite being nonflammable.

Our approach is focused on the use of large fractions of high flash point (or no flash point) fluorinated ether co-solvents to make inherently nonflammable electrolytes, as seen in Table 3. The key to this approach is that the FR can be used in large enough quantity to ensure nonflammability of the entire electrolyte formulation. The idea of ether co-solvents was first reported by Arai using methyl nonafluorobutyl ether. [54, 55] Following this, Chen, *et al.* [65] used Allyl tris(2,2,2-trifluoroethyl) carbonate (ATFEC) as cosolvent, but it is not clear if the solvent showed no Fp. However, the results seem to indicate that the ATFEC reduces flammability of the electrolyte. Several years later Naoi, *et al.* [57] have shown in small capacity cells that hydrofluoro ethers (HFE) were thermally stable. The objective of this work is to continue the work on hydrofluoro ether (HFE) co-solvents in lithium-ion electrolytes to increase the total solvent flash point in an effort to mitigate flammability. A second objective is to replace $LiPF_6$ in our electrolyte design with lithium sulfonimide salts in an effort to improve the overall thermal stability and safety of the electrolyte [58].

The structure of HFEs electrolytes investigated are shown in Figure 1. These liquids are "Engineered" fluids developed by 3M as a replacement for perfluorocarbons (PFCs) and perfluoropolyethers (PFPEs) and for use in heat transfer applications.

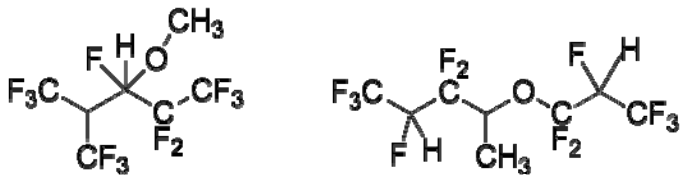

Figure 1. Chemical structures for 2-trifluoromethyl-3-methoxyperfluoropentane (TMMP) (left) and 2-trifluoro-2-fluoro-3-difluoropropoxy-3-difluoro-4-fluoro-5-trifluoropentane (TPTP) (right) hydrofluoro ethers used for evaluation.

In addition, we studied the conventional electrolytes containing either EC:EMC (3:7 w%) and 1.2M $LiPF_6$ or EC:DEC (5:95 v%) and 1M $LiPF_6$ as electrolytes. These are designated as "baseline" or "standard" electrolytes. The amount of HFE in the electrolytes is 50% by volume which is significant compared to the percent used for FR additives (typically <<20 v%). Electrolyte formulations evaluated in this work are listed in Table 5.

Table 5. Electrolyte composition.

	Solvent					Salt- 1M	ID
	TMMP	TPTP	EC*	DEC**	EMC***		
Composition v%	30		5	35	30	LiBETI	EC:DEC:EMC:TMMP-1M LiBETI
	50		5	45		LiBETI[a]	EC:DEC:TMMP-1M LiBETI
		50	5	45		LiBETI[a]	EC:DEC:EMC:TPTP-1M LiBETI
		50	5	45		$LiPF_6$	EC:DEC:EMC:TPTP-1M $LiPF_6$
		50	5	45		LiTFSI[b]	EC:DEC:EMC:TPTP-1M LiTFSI
			5	95		$LiPF_6$	EC:DEC-1M $LiPF_6$
			55	45		$LiPF_6$	EC:DEC(55:45)-1M $LiPF_6$
Composition w%			30		70	1.2M $LiPF_6$	EC:EMC-1.2M $LiPF_6$
Flash point	No	No	Yes	Yes	Yes		

* Ethylene carbonate; ** Diethyl Carbonate; *** Ethyl Methyl carbonate a=Lithium Bis (Perfluoroethyl sulfonyl)imide; b=Lithium trifluoro sulfonimide

As an interesting side note, we started by just increasing the amount of EC in the electrolyte, since the F_p of EC is 145 °C (significantly greater than the linear carbonates). We compared the effect of the amount of EC on the flammability and freezing point of the electrolyte. For example, EC:DEC (5:95 v%)-1M $LiPF_6$ was flammable whereas EC:DEC (55:45 v%)-1M $LiPF_6$ electrolyte was nonflammable. However, the freezing point of EC:DEC (55:45 v%)-1M $LiPF_6$ was measured to be -5 °C while EC:DEC (5:95 v%)-1M $LiPF_6$ remained liquid even at -50 ºC.

2.4. Evaluation of HFE electrolytes

2.4.1. Electrochemical characterization

The electrolytes were characterized for conductivity and electrochemical voltage stability using a commercial 2-electrode cell with a cell constant (K) of one [58]. Before measuring conductivity of the organic electrolytes, the conductivity of a KCl standard solution was measured to verify the cell constant was unity. The conductivity of the KCl standard at 25 °C computed from the measured resistance, using a value of 1 for K, was identical to that certified by the National Institute of Standard and Technology for that concentration of the KCl solution. After measurement, the cell was cleaned, rinsed with deionized water and dried in an oven overnight before using it for measuring conductivity of the organic electrolytes. Electrolyte resistance was measured in the frequency range 10^6 – 0.1 Hz using a Solartron SI 1287 Electrochemical Interface coupled with a Solatron SI 1260 Impedance Phase Analyzer and controlled with Zplot software. The x-intercept was used to determine the electrolyte resistance and the reciprocal of

this value gives conductivity. The conductivity values at different temperatures for the different electrolytes are given in Figure 2. Figure 3 shows the electrochemical voltage stability window for a couple of electrolytes (EC:EMC-1.2M LiPF6 and EC:DEC-TPTP-1M TFSI). Other electrolytes also show similar voltage window [58]. The electrolytes exhibit stability over a 5 V range which could be attractive for high voltage nickel-doped spinel cathode cells. The presence of large fractions of HEFs does not diminish the voltage window of the electrolyte.

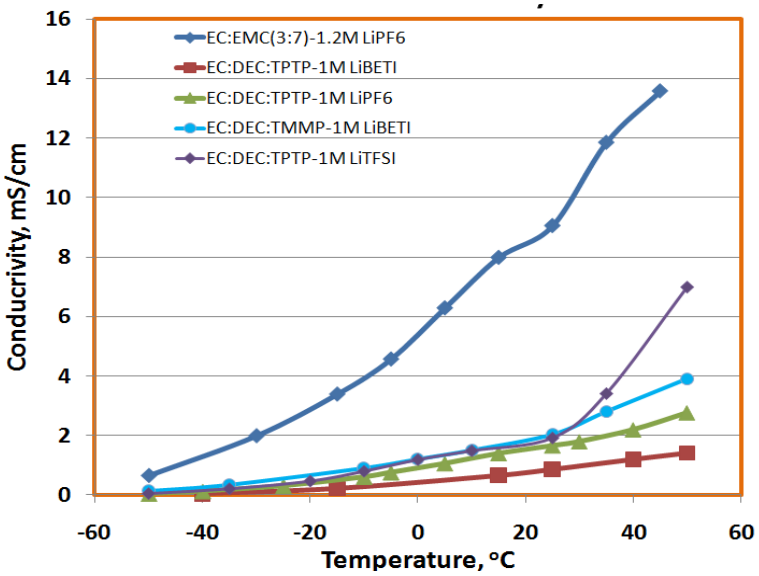

Figure 2. Conductivity of different electrolytes at different temperatures.

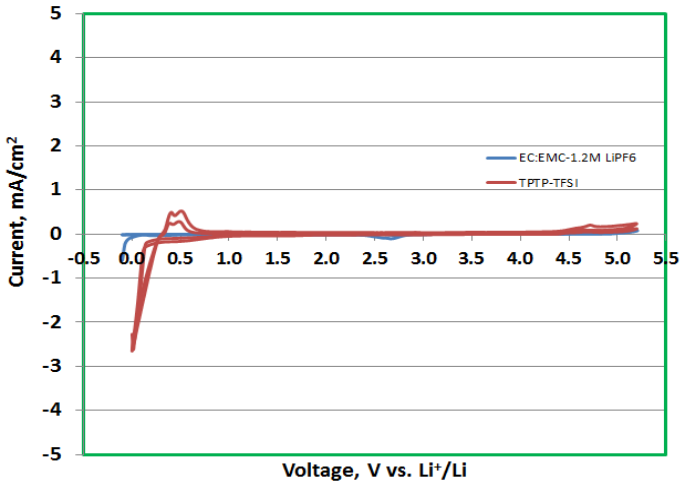

Figure 3. Electrochemical voltage stability window for electrolytes measured at a scan rate of 1 mV/s in a three electrode cell with a platinum working electrode.

2.4.2. Fabrication of 18650 cells

Lithium-ion cell electrodes (cathodes and anodes) were coated and fabricated 18650 cells using our in-house facility for all full cell evaluations [66]. These cells contain $LiMn_{0.33}Ni_{0.33}Co_{0.33}O_2$ (NMC 111) cathode active materials and a carbon intercalation anode. Cathode composition is 94 w% NMC active material, 3 w% PVDF, and 3 w% conductive carbon. Anode composition is 92 w% intercalation carbon active material, 6% PVDF and 2 w% conductive carbon. Cathodes were coated with a total electrode loading of 15 mg cm^{-2} per side (30 mg cm^{-2} double sided), which resulted in cathodes that were approximately 145 µm thick including the 17 µm aluminum current collector. Anodes were coated with a total electrode loading of 6.5 mg cm^{-2} per side (13 mg cm^{-2} double sided), resulting in anodes that were approximately 150 µm thick including the 22 µm thick copper current collector. Electrode fabricated for testing have specific capacities of 150 mAh g^{-1} for cathodes and 350 mAh g^{-1} for anodes (based on coin cell data vs. lithium). The cells have a total negative to positive ratio of approximately 1.12. Upon fabrication, a standard formation cycling protocol was used for all cells, as seen in (
Figure 4).

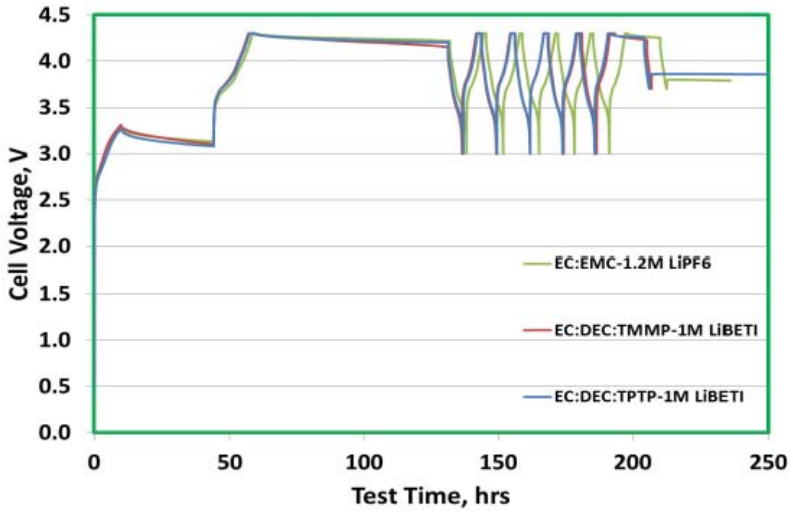

Figure 4. Comparison of 18650 formation cycles for different electrolytes.

The performance of cells with the HFE electrolytes is comparable to that of the baseline and the electrolytes are stable against the NMC cathode. After formation these cells were cycled for capacity and Figure 5 shows cell capacity vs. cycle number for TPTP, TMMP, and baseline EC:EMC electrolytes. Although the baseline (green) initially exhibits 15% higher capacity than the HFE cells, the fade rate of the baseline cells is higher and the cell discharge capacities begin to converge at 70 cycles. While this is limited cycle data, it does suggest reduced capacity fade with the HFE electrolytes and that any penalty in performance of the fresh cells with HFEs may not be as significant over the life of the cell.

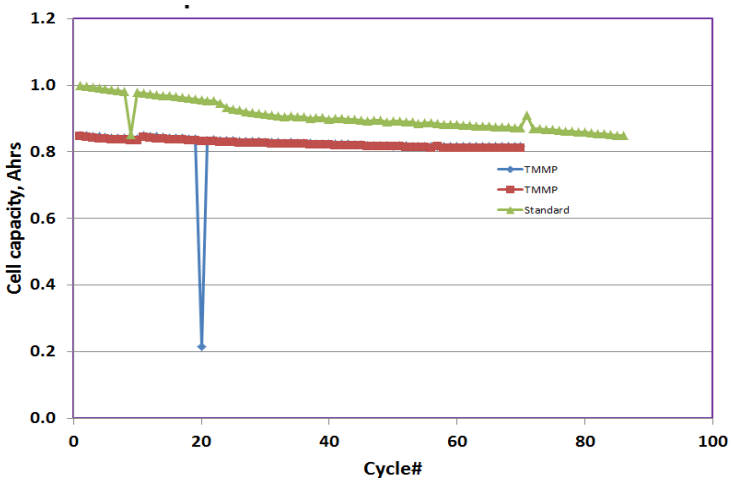

Figure 5. Capacity vs. cycle # for SNL-built 18650 cells containing different electrolytes.

2.4.3. Calorimetry measurements of HFE electrolytes

The thermal stability of the HFE and carbonate electrolytes were measurement by differential scanning calorimetry (DSC) and accelerating rate calorimetry (ARC). Figure 6 shows heat flow (W/g) as a function of temperature for EC:DEC:TPTP-1M LiBETI, EC:DEC:TPTP-1M $LiPF_6$, and EC:EMC-1 M $LiPF_6$ electrolytes. Results show an endotherm for $LiPF_6$ melting at 240-250 C for the LiPF6 electrolytes followed by a broad exotherm at 275-300 °C. The LiBETI electrolyte (blue trace) shows a much higher onset temperature for melting/decomposition > 350 °C. This suggests improved thermal stability with the sulfonimide salt with no adverse temperature instabilities associated with the HFE in the electrolytes.

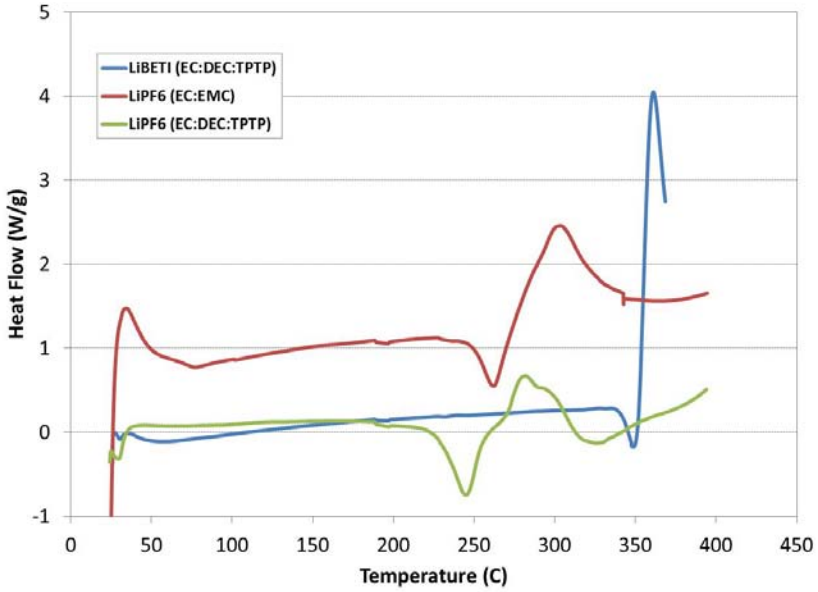

Figure 6. DSC measurements of heat flow (W/g) as a function of temperature for HFE/sulfonimide and carbonate/$LiPF_6$ electrolytes.

Accelerating rate calorimetry (ARC) was used to measure the total gas volume generated due to electrolyte decomposition for the electrolytes. In this measurement, electrolytes are heated in a closed fixed volume and the resulting decomposition gas pressure is converted to gas volume at standard temperature and pressure (STP). Figure 7 shows volume of gas evolved vs. temperature and the onset of gas evolution. The black and red traces are the baseline electrolytes and the remaining traces are electrolytes containing HFEs. The volume of gas generated for the HFE electrolytes is approximately half of the volume generated by the baseline electrolytes. Additionally, the onset temperature for gas generation is shifted from ~160 ºC for the LiPF6 electrolytes (both baseline carbonate and HFE solvents) to ~240 ºC for the lithium sulfonimide electrolytes. Results suggest that total gas volume is governed by the solvent system and the onset temperature for electrolyte decomposition to form gas products is a function of the electrolyte salt.

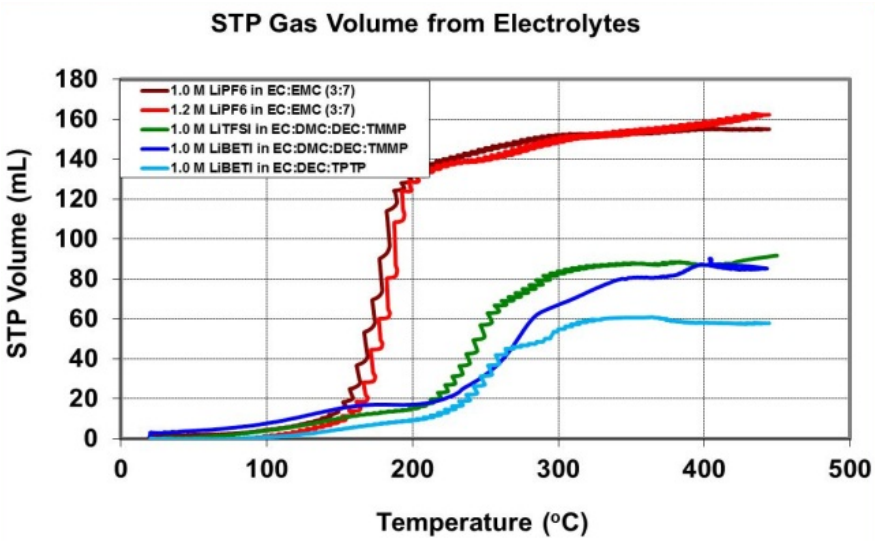

Figure 7. Volume of gas generated vs. temperature.

ARC measurements were also made on full 18650 cells (NMC/graphite) with the baseline and HFE electrolytes. Figure 8 shows the ARC profiles for EC:DEC:TMMP-1 M LiBETI, EC:DEC:TPTP-1 M LiBETI, and baseline EC:EMC 1.2 M $LiPF_6$ cells. The onset temperature for the high rate runaway reaction is approximately 15 °C lower for the HFE cells relative to baseline cells, but the peak heating rates and total enthalpies are comparable. Figure 9 compares the total gas volume generated as a function of temperature for cells during the same ARC experiments. At the end of thermal runaway, the HFE cells show a ~60% reduction in total gas volume. These gas volume results for cells are consistent with the observations made for just the thermal deposition of electrolyte alone (Figure 7).

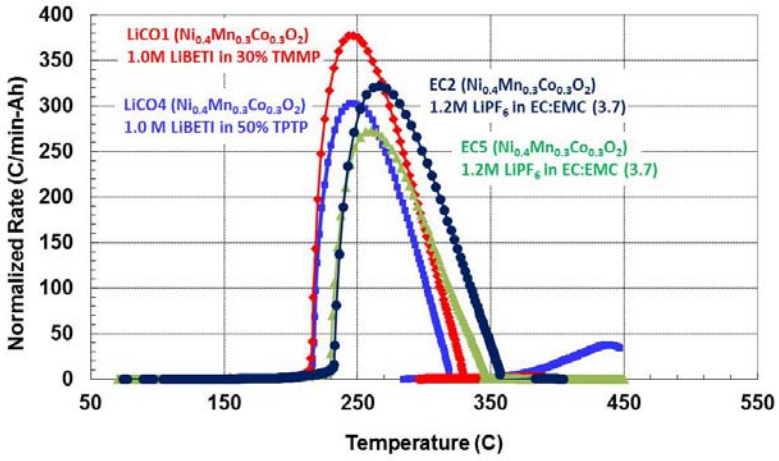

Figure 8. ARC profile for NMC 433/graphite cells with HFE and carbonate electrolytes.

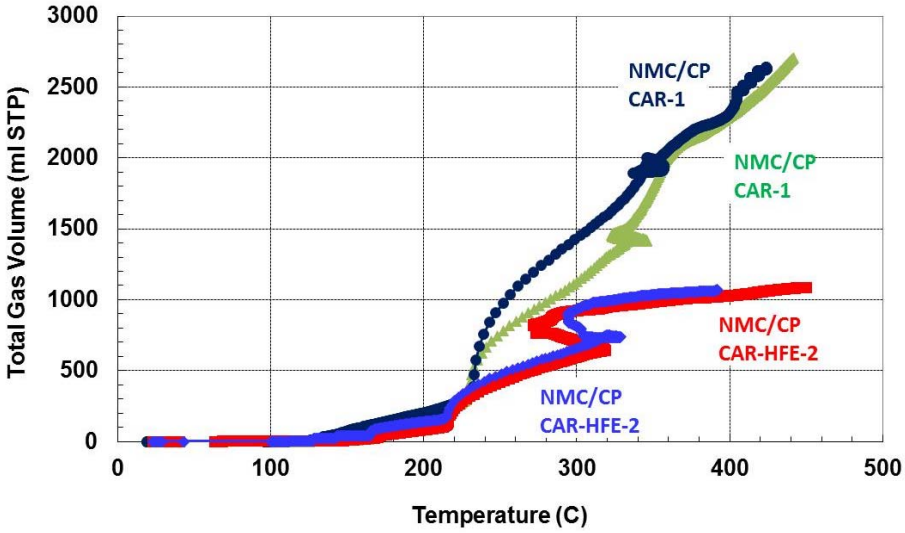

Figure 9. HFE electrolytes in 18650 NMC 433/graphite cells show lower gas volume than the baseline.

2.5. Flammability measurements

As described above, work on flame retardant additives and nonflammable electrolytes for lithium-ion batteries has suffered because of the lack of a meaningful tests for electrolyte flammability. Much of the previous work on FRs relies on testing standards for solvent flammability. These include standard procedures from the American Society for Testing and Materials (ASTM), Underwriters Laboratories (UL), and International Electrotechnical Commission (IEC) such as ASTM D-5306, ASTM D2863, UL-94VO, and IEC 62133 to compute both the self-extinguishing time (SET) and the limited oxygen index (LOI) to evaluate the flammability of the electrolytes. The shorter the SET and higher the LOI (this is the % of

oxygen needed in the O_2/N_2 mixture to keep the electrolyte burning for at least 60s) the less flammable the electrolyte is. In general, the electrolyte with the additives showed shorter SET and higher LOI than the electrolyte without FR. Descriptions of the thrust of the different ASTM and UL tests were discussed in depth by M. Otsuki, *et al.* [42].

While these techniques are certainly appropriate for measuring solvent flammability in general, they do not adequately test flammability for electrolytes in lithium-ion cells. The primary driver for an improved flammability test is that these existing standard tests do not test electrolyte flammability under common failure mode conditions for lithium-ion cells which include venting solvent vapor, liquid solvent, and decomposition products at elevated temperature and pressure which can dramatically affect the test results. In addition, much of the FR development work focuses on characterization and testing (calorimetry and flammability) the FR only and not the FR with the electrolyte solvent.

Flammability measurements are made for both electrolyte alone and electrolyte in full 18650 cells in the fixture shown in Figure 10. Either 5 mL of electrolyte sealed in an 18650 can or an 18650 cell is placed in a brass heater fixture. The electrolyte sample or cell is heated at 5 C/min until the vapor pressure in the can exceed the burst disc pressure causing electrolyte to vent. Electrolyte is vented directly into an ignition source 2” above the header.

Figure 10. Experimental setup showing: a) picture of the copper heater block used and b) line drawing of the experimental setup.

Table 6. Electrolyte measurements for carbonate and HFE based electrodes.summaries the electrolyte flammability measurements made for carbonate and HFE electrolytes using this technique.

Table 6. Electrolyte measurements for carbonate and HFE based electrodes.

Electrolyte Solvent	Ignition	Δt (vent-ignition)	Burn time (s)
EC:DEC (5:95 v%)	Yes	< 1	36
EC:DEC (5:95 v%)	Yes	1	63
EC:EMC (3:7 w%)	Yes	5	6
EC:EMC (3:7 w%)	Yes	3	12
EC:DEC:EMC:TMMP (5:35:30:30 v%)	Yes	3	14
EC:DEC:EMC:TMMP (5:35:30:30 v%)	No	NA	NA
EC:DEC:EMC:TMMP (5:35:30:30 v%)	Yes	1	27
EC:DEC:EMC:TMMP (5:35:30:30 v%)	No	NA	NA
EC:DEC:TPTP (5:45:50 v%)	No	NA	NA
EC:DEC:TPTP (5:45:50 v%)	No	NA	NA
EC:DEC:TPTP (5:45:50 v%)	No	NA	NA
EC:DEC:TPTP (5:45:50 v%)	No	NA	NA
EC:DEC:TMMP (5:45:50 v%)	No	NA	NA
EC:DEC:TMMP (5:45:50 v%)	No	NA	NA
EC:DEC:TMMP (5:45:50 v%)	No	NA	NA

The all carbonate electrolytes with the lowest flash points all ignited and burned under these test conditions. Interestingly, the EC:DEC (5:95 v%) sample ignited the fastest and burned for the longest period of time which is consistent with that electrolyte containing the largest fraction of low Fp linear carbonate. At 50% HFE, none of the samples with TMMP or TPTP showed any ignition or flammability. There appears to be an inflection point in the flammability behavior at 30% HFE observed for EC:DEC:EMC:TMMP (5:35:30:30 v%) electrolytes. Two of the four samples evaluated showed ignition and flammability and two did not. There is clearly a need for a systematic evaluation of flammability as a function of % HFE to better understand the ignition properties of these complex systems.

Figure 11-Figure 14 show still images of the flammability tests from the digital video files for several different electrolyte samples just after the cell vent and ignition for the carbonate electrolytes and just after the cell vent with no ignition for the HFE electrolytes.

Figure 11. EC:EMC (3:7 w%)-1.2M $LiPF_6$ is mildly flammable.

Figure 12. EC:DEC (5:95 V%)-1M $LiPF_6$ is violently flammable.

Figure 13. EC:DEC:TMMP (5:45:50 v%)-1M LiBETI is nonflammable.

Figure 14. EC:DEC:TPTP(5:45:50 v%)-1M LiBETI is nonflammable.

These data clearly show that at 50% HFE (wt%) the electrolytes do not ignite and are nonflammable under these test conditions. To validate these results in full cells, NMC 18650 cells were built with both the EC:DEC:TMMP(5:45:50 wt%) and the EC:DEC:TPTP(5:45:50 wt%).

When tested from flammability the TPTP cell vented at 150 °C, went into thermal runaway but did not ignite. Still images from the video are shown in Figure 15 and no ignition is observed. In fact, the observed thermal runaway reaction for the TPTP cell was quite mild with a peak temperature of ~ 250 °C (Figure 16). This result is consistent with observations made for TPTP electrolyte alone where no ignition was observed. During the test of the TMMP cell, the cell shorts internally at 110 °C (which corresponds to the shrinkage temperature of most poly(olefin) separators), self-ignites, goes into a high order thermal runaway (Figure 17 and Figure 18). The cell peak temperature is > 350 °C during the runaway reaction. Results of this test are somewhat convoluted by the shorting of the cell and highlights one of the key failure modes of lithium-ion cells related to separator failure and is described in detail later in this report. More work needs to be done to determine the ignition characteristics of TMMP in full cells and how cell self-ignition due to internal shorting effects flammability of electrolyte solvents.

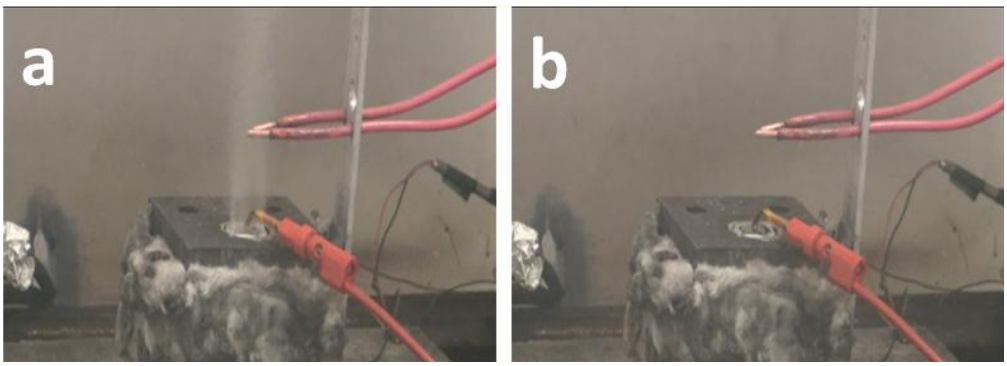

Figure 15. Thermal ramp test of full cell containing TPTP. This is nonflammable.

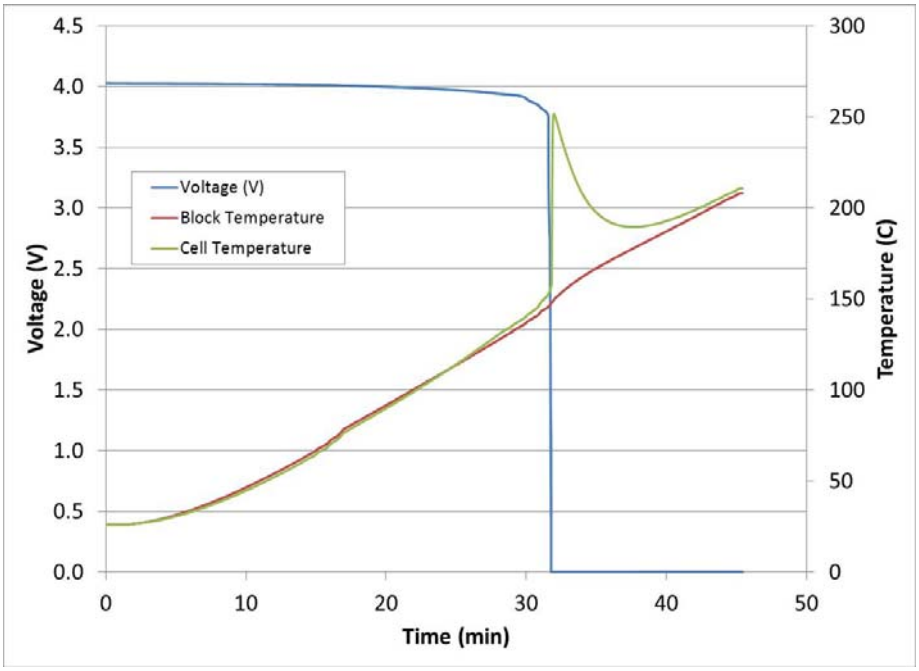

Figure 16. Voltage and temperature data for the TPTP cell during the thermal ramp test.

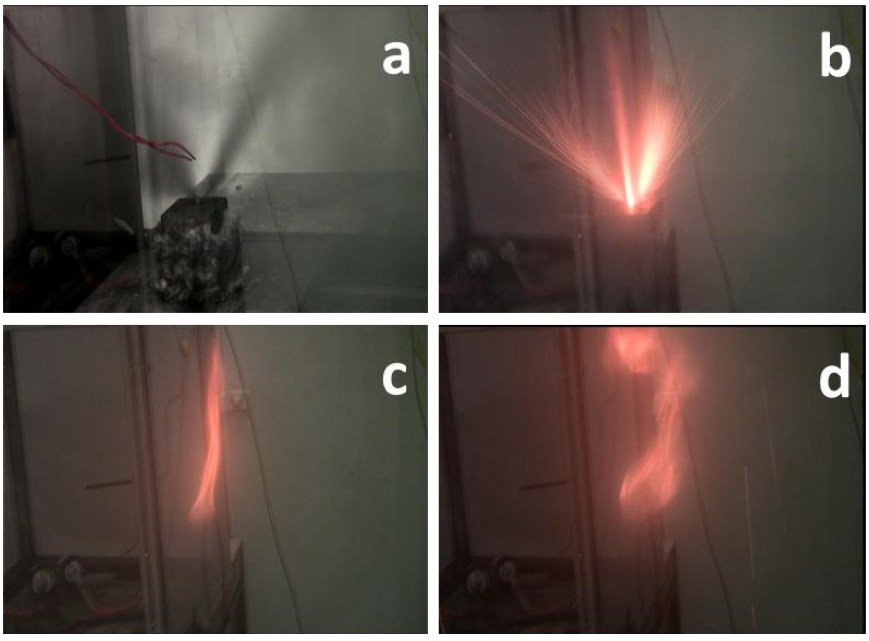

Figure 17. Thermal ramp test of full cell containing TMMP.

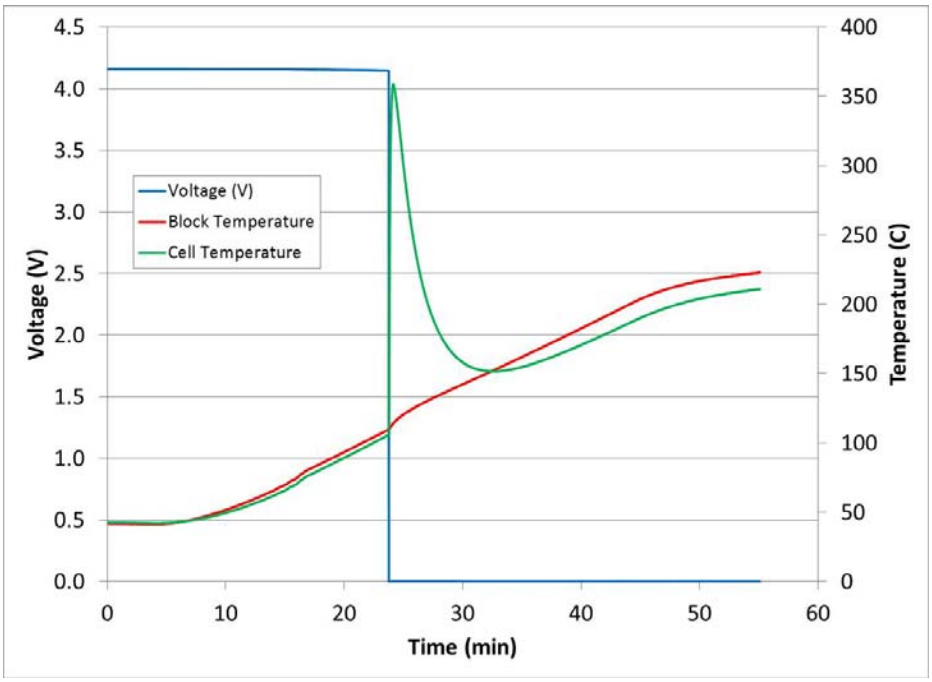

Figure 18. Voltage and temperature data for the TMMP cell during the thermal ramp test.

2.6. Autoignition measurements

In conjunction with the cell vent flammability test, it is also important to understand the fundamental ignition properties of lithium-ion battery electrolytes as potential fuels. As mentioned above, traditional measurements of ignitability of liquid compounds rely on historical testing standards. Determining a liquid auto-ignition temperature done in accordance to the standardized ASTM procedure, ASTM E659 ("Standard Test Method for Auto-ignition Temperature of Liquid Chemicals"). This procedure consists of injecting 100–250 µL of the compound in question into a preheated 500 mL glass flask that resides within a temperature-controlled furnace and then visually observing whether or not a flame is evident over the next 10 minutes. The temperature is then adjusted until the characteristic temperature at which a flame is first evident is denoted as the auto-ignition temperature. In this procedure, there is no attempt to control (a) the degree of premixing of the vaporized compound and the surrounding air (i.e. of the fuel-air equivalence ratio), (b) the characteristic residence time of the fuel-air mixture within the furnace hot zone (before natural convection conveys the mixture out into the cool ambient), or (c) the relative visibility of flames produced from carbonated compounds compared to traditional hydrocarbon fuels, for example. All of these shortcomings lead to questions regarding the reliability of this test method for determining the actual ignition tendency of different electrolytes. The long timescale of the ASTM auto-ignition test method (10 min.) also has limited utility for assessing immediate flammability risk associated with Li-ion battery failure, and different volatility of different solvent mixtures could lead to anomalous results when using the ASTM technique. The auto-ignition temperatures that have been reported for typical solvent constituents (on chemical suppliers' MSDS forms) are indicated in Table 7, along with their molecular formula and molecular weight.

Table 7. Reported auto-ignition temperatures of solvents.

Solvent component	Reported T_{ig} (°C)	Molec. Formula	MW (g/mol)
di-methyl carbonate (DMC)	458	$C_3H_6O_3$	90.08
diethyl carbonate (DEC)	445	$C_5H_{10}O_3$	118.13
ethyl methyl carbonate (EMC)	440	$C_4H_8O_3$	104.10
ethylene carbonate (EC)	465	$C_3H_4O_3$	88.06
TMMP	408	$C_7H_3F_{13}O$	350.09
TPTP	297	$C_8H_6F_{12}O$	346.13

In this project, we have developed a new procedure for determining the auto-ignition time delay as a function of temperature under controlled stoichiometry conditions. This is accomplished through the preheating of air and of the compound in question before rapid mixing of the compound or solvent mix into the air in a heated flow tube (to minimize wall effects). Evidence of exothermic chemical reactions (i.e. 'ignition') is provided through thermocouples imbedded in the gas flow and by on-line chemical analysis of the gases leaving the flow chamber. A particular focus of our work is on ascertaining the utility of using the hydrofluoro ether compounds TMMP and TPTP to reduce the risk of battery ignition. These compounds do not have a flash point (on account of their very heavy molecular weight) and therefore are not considered flammable in their liquid state at room temperature. However, once they are vaporized, they can ignite, as evidenced by the reported auto-ignition temperatures according to the ASTM procedure. In fact, their reported auto-ignition temperatures are lower than those of the conventional battery solvents. We aim to clarify this behavior under the vapor ignition conditions likely to be present during the thermal runaway failure mode of Li-ion cells.

An electrically heated flow reactor was used to investigate the ignition characteristics of various electrolyte constituents. A schematic of the experimental configuration is shown in Figure 19 and a photograph of the configuration is shown in Figure 20. In these experiments, an HPLC pump delivered controlled amounts of liquids into an electrically heated vaporizer. In order to avoid re-condensation of the test compound(s), the vaporizer outlet temperature was electronically controlled to 60-100K above the liquid's boiling point and heated, insulated line carried the vapor to the flow reactor. In the bottom of the flow reactor, the flow gas (either dry air or nitrogen) was heated to the reactor setpoint temperature by passing through a bed of stainless steel beads capped by a stainless steel disk with 20 evenly distributed holes (1mm diameter). Similarly, the electrolyte vapor was preheated to the same setpoint temperature by passing the fuel vapor tube through the center of the beads. The heated fuel enters the cylindrical reaction chamber (6.68 inches long, with a 1.75 inch ID) in the centerline of the chamber through radial outlets that promote rapid mixing with the axial flow of air. A relatively wide cylindrical volume was used for these tests on the basis of previously measured auto-ignition temperature dependence on the cylinder width (i.e. on the surface-to-volume ratio of the reaction volume) [67]. This previous experience suggests a cylindrical width of approximately one inch is required to make the measurement of auto-ignition temperature insensitive to wall effects. In fact, an

earlier version of the experiment during this project in which smaller diameter flow cells were used showed strong resistance to full ignition and could not give results for simple hydrocarbon fuels that were consistent with the literature or computed ignition delay times. Stainless steel (as used here) or glass reactor walls are also recommended in the cited report to minimize wall effects.

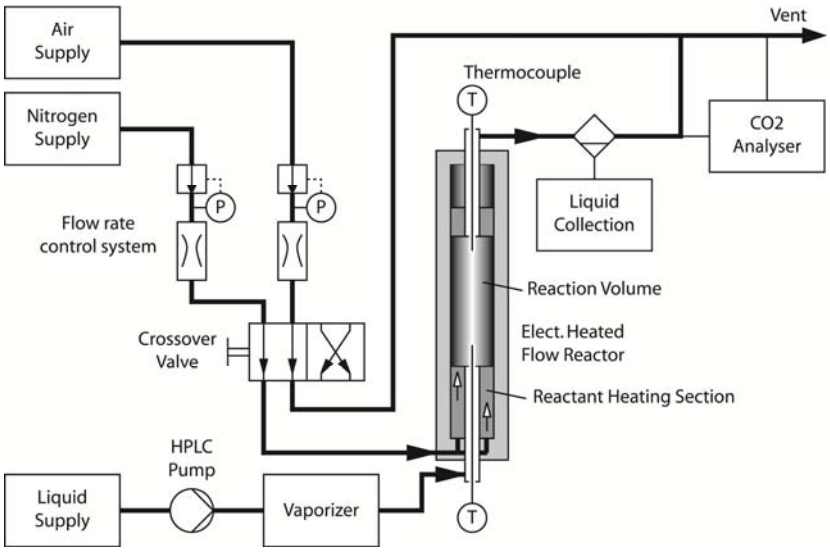

Figure 19. Schematic of the experimental setup for auto-ignition tests.

To evaluate the ignition properties of the chosen compound, a flow of nitrogen would be established, for a given temperature, based on a predetermined (chosen) residence time in the reactor. Then the fuel (electrolyte) compound flow would be established at a flow rate corresponding to the chosen overall equivalence ratio. Once the fuel flow rate was established, the nitrogen flow would be switched to air and the response of two thermocouples (one in the reactor volume near its inlet and one near its outlet) would be monitored for signs of heat release. Furthermore, the gas analyzer CO_2 measurement would be interrogated for signs of CO_2 production. For the carbonated solvent compounds, some thermal decomposition of the solvent would apparently occur under the test conditions, as measurable concentrations of CO_2 would be present even before any O_2 (in the form of air) was introduced into the reaction chamber (i.e. when the hot solvent vapor was simply mixing with hot nitrogen). Once the air flow had been operating for a time equivalent to six times the flow time through the reactor volume, the air flow was switched off and replaced by nitrogen, and the baseline thermocouple and gas analyzer readings were recorded, for comparison with the values before air had been injected. Reactor volume gas temperatures were observed to differ by no more than 8 K during such tests.

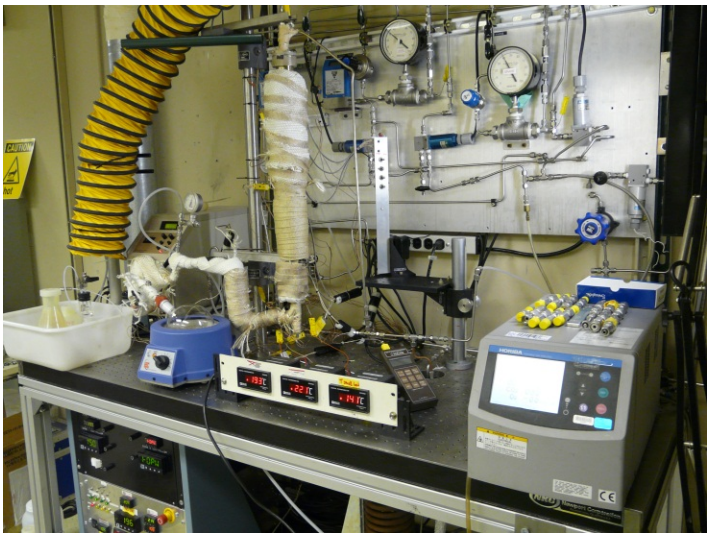

Figure 20. Photograph of the experimental setup, with liquid supply and HPLC pump to the left, insulated reactor tube in the middle, and gas analyzer to the right.

Most ignition tests were conducted with an equivalence ratio of 1.6 (somewhat fuel rich). This stoichiometry was chosen because it is close to the optimum stoichiometry for ignition (which is always somewhat fuel-rich). Also, assuming solvent ignition typically occurs within the battery cell itself, one would generally expect fuel-rich conditions to exist at the point of ignition. The absolute value of the auto-ignition temperature is not very sensitive to stoichiometry, so this choice does not distort the data in any way. In fact, for DEC some experiments were conducted with an equivalence ratio of 0.5 (fuel-lean), and identical trends were found as for the fuel-rich cases, with a difference in the effective ignition temperature of about 5 K.

2.6.1. n-hexane

Before characterizing the auto-ignition behavior of the battery solvents, the auto-ignition of n-hexane was investigated, as a means of validating the performance of the experimental setup. N-hexane has a well-developed detailed chemical kinetic mechanism for predicting low temperature ignition [68]. This mechanism can then be used in the Homogeneous Reactor Calculation in CHEMKIN-PRO to predict ignition delay times for given reactor compositions and temperatures. Figure 21 shows a summary of the experimental data and corresponding modeling results from CHEMKIN-PRO. The experimental data are shown as symbols of three different types: filled symbols indicate the occurrence of clear, strong ignition, open symbols indicate no evidence of ignition, and the ringed symbols indicate evidence of weak ignition. As the occurrence of ignition at the ignition limit is inherently a probabilistic event, sensitive to minute variations in flow rates, temperatures, etc., there is some overlap amongst the different symbol types for a given reactor condition. The characteristic ignition temperature determined by the experiments for a given flow time (i.e. ignition delay time) is best thought of as being somewhere in the middle of the distribution of weak ignition events. On this basis, the comparison with model predictions show that the experimental results are in good agreement for short ignition delay times (below approximately 10 s). For longer ignition delays, higher mixture

temperatures are required experimentally for ignition than are predicted by the CHEMKIN results. This most likely reflects the small flow rates used for these conditions and increased heat loss to the reactor wall during the long residence time of the reaction products in the reaction chamber (based on the radius of the reaction chamber a characteristic time scale for heat conduction for air at 250 °C is about 8 s, thus comparable to the characteristic residence time for reactants in the vessel). All enclosed ignition experiments inherently suffer from this problem at sufficiently long residence times. The result here suggests that for temperatures on the order of 300 °C, our flow reactor gives trustworthy results up to a residence time of 10 seconds.

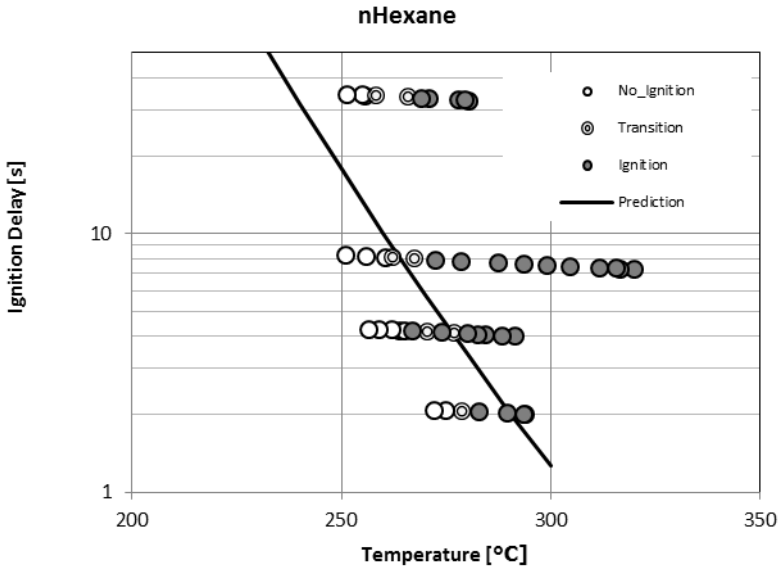

Figure 21. Modeled and measured ignition delays for fuel-rich mixtures of n-hexane in air.

2.6.2. Diethyl carbonate (DEC)

The ignition tests of DEC showed that somewhat higher temperatures are required to ignite DEC than to ignite n-hexane. However, the measured ignition temperatures are much lower than those indicated by the ASTM auto-ignition test for DEC, with a reported auto-ignition temperature of 445 °C. As shown in Figure 22, the DEC ignites around 280 °C with a 10 s ignition delay and at 310 °C with a 3 s ignition delay.

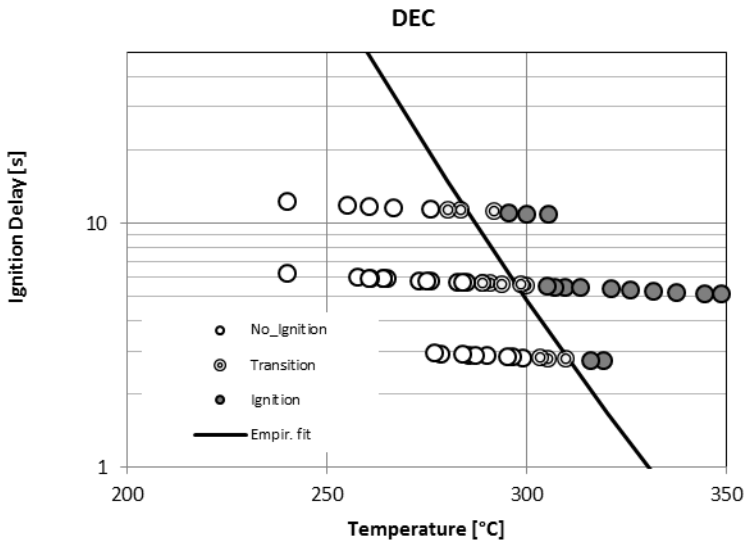

Figure 22. Measured ignition delays for fuel-rich mixtures of diethyl carbonate and air. The curve shown is an approximate Arrhenius fit of measured ignition delay time vs. temperature.

2.6.3. Ethyl methyl carbonate (EMC)

Ignition of EMC in air mixtures is found to occur at somewhat higher temperatures than for DEC. Figure 23 shows that fuel rich mixtures ignite around 300 °C with a 10 s ignition delay and 335°C with a 3 s ignition delay. The CO_2 measurements in the solvent-N_2 flow indicate that EMC has a higher tendency to decompose than DEC at elevated temperatures. Interestingly, the ASTM auto-ignition temperature of EMC is slightly *lower* than that of DEC, though still at a value (440 °C) much greater than seen here.

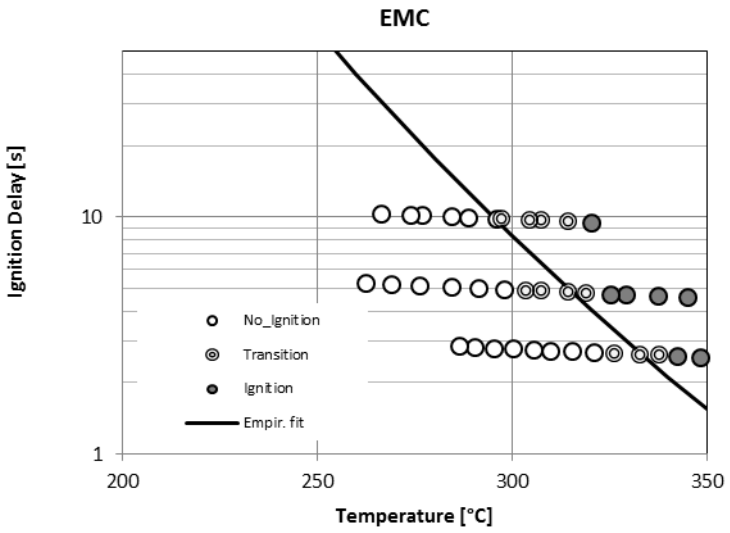

Figure 23. Measured ignition delays for fuel-rich mixtures of ethyl methyl carbonate and air. The curve shown is an approximate Arrhenius fit of measured ignition delay time vs. temperature.

2.6.4. Ethylene Carbonate (EC)

Figure 24 summarizes the ignition test results for fuel-rich mixtures of ethylene carbonate with air. Only a limited amount of data was collected with EC, on account of difficulties in keeping this compound in a liquid state as it was pumped (its melting point is 36 °C). From the collected data, it appears that the ignition temperature of EC is virtually identical to that for EMC, with an auto-ignition temperature of approximately 315 °C for a 7 s ignition delay. The ASTM test gives a substantially higher value for the auto-ignition temperature (465 °C) than for the other standard electrolytes.

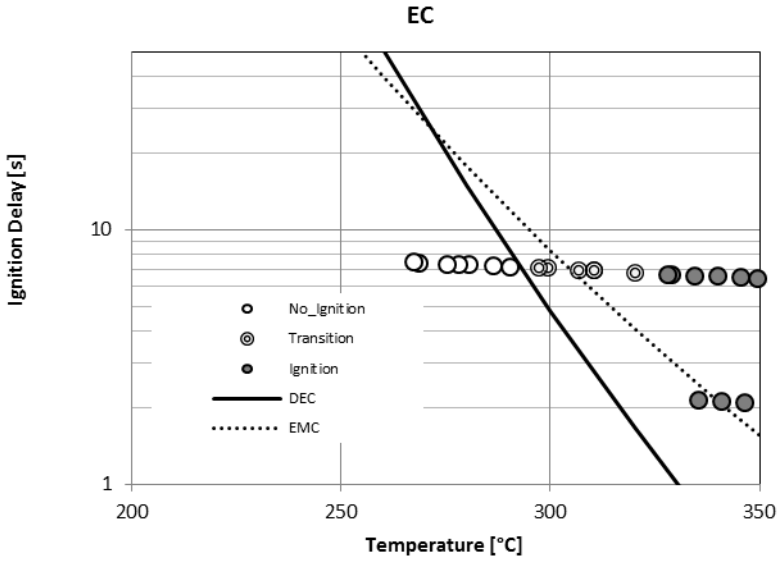

Figure 24. Measured ignition delays for fuel-rich mixtures of ethylene carbonate and air. The curves shown are approximate Arrhenius fit of measured ignition delay time vs. temperature for DEC and EMC.

2.6.5. TMMP

Figure 25 clearly indicates that this hydrofluoroether compound (2-trifluoromethyl-3-methoxyperfluoropentane) ignites at much higher temperatures than the traditional battery solvents. At 5 sec residence time the fuel rich mixture ignites only at temperatures above 440 °C, almost 150 °C higher than the other electrolytes. The ignition delay is less sensitive to the initial reactant temperature, which is reflected by a much higher activation temperature in the empirically fit Arrhenius equation. Also, the CO_2 measurements do not give any evidence of thermal decomposition of this compound for the investigated temperatures (exceeding 450 °C). If one extrapolates the current results out to long residence times (order of 1 min.), they appear to be in agreement with the reported ASTM auto-ignition temperature of 408 °C.

2.6.6. TPTP

Figure 26 summarizes the ignition test results for fuel-rich mixtures of TPTP (2-trifluoro-2-fluoro-3-difluoropropoxy-3-difluoro-4-fluoro-5-trifluoropentane) with air. This compound shows somewhat greater ignition tendency than TMMP, especially at longer ignition delay times. However, even at very long residence times the reported auto-ignition temperature of 297 °C appears to be in error. Similar to TMMP there is no evidence of thermal decomposition of TPTP even at temperatures above 450 °C.

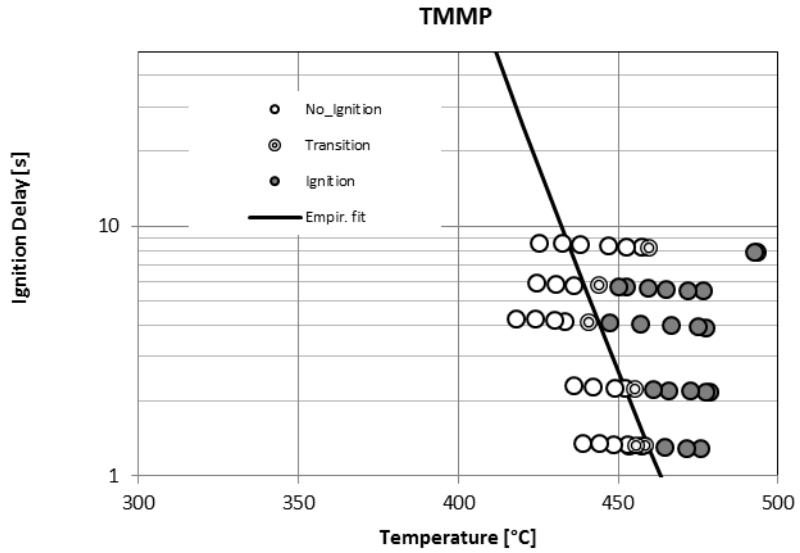

Figure 25. Measured ignition delays for fuel-rich mixtures of TMMP and air. The curve shown is an approximate Arrhenius fit of measured ignition delay time vs. temperature.

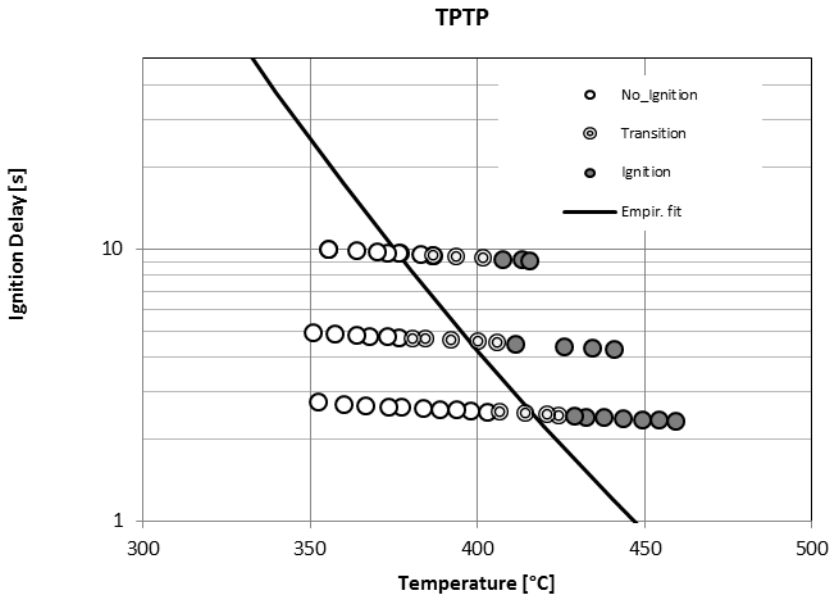

Figure 26. Measured ignition delays for fuel-rich mixtures of TPTP and air. The curve shown is an approximate Arrhenius fit of measured ignition delay time vs. temperature.

2.6.7. Pure solvent comparison

Figure 27 gives a summary of the indicated ignition delays for the various pure solvent components as a function of temperature. For simplicity, only the approximate Arrhenius fits of the experimental data are shown and the limited results for EC (which overlapped those for EMC) are not shown. The increased resistance to ignition of the hydrofluoroether compounds is clearly evident.

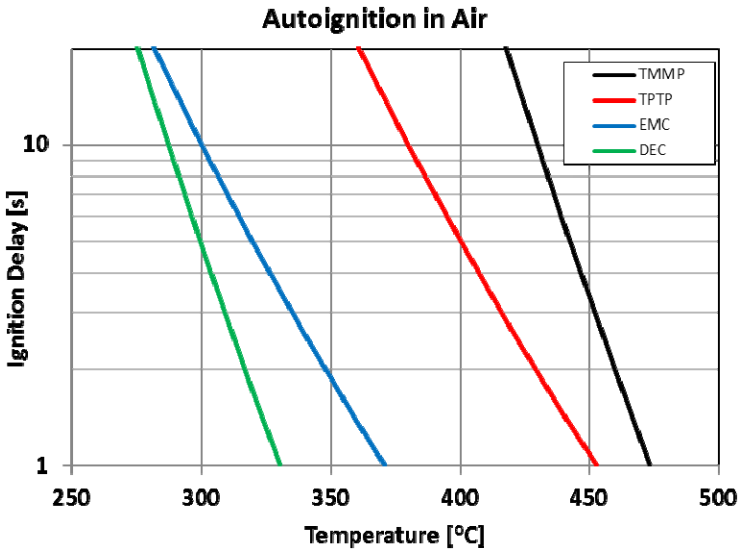

Figure 27. Approximate Arrhenius fits of measured ignition delay times vs. temperature for various pure solvent components.

2.6.8. EC:DEC:TMMP=5:45:50 by wt.

In addition to investigating the ignition delays of pure compounds, specified solvent mixtures of EC, DEC, and hydrofluoroether compounds were investigated, with 5% EC and 45% DEC (by weight). Note that the hydrofluoroether compounds have much higher molecular weights than the traditional carbonated solvents, such that a 50 wt-% mixture with the hydrofluoroether compound corresponds to a small molar component. Figure 28 summarizes the ignition test results for fuel-rich mixtures of EC:DEC:TMMP with air. Only moderately higher ignition temperatures are found from adding this amount of TMMP, as might be expected based on the relatively small volumetric contribution of the TMMP vapor to the overall solvent mixture (25%).

2.6.9. EC:DEC:TPTP=5:45:50 by wt.

Use of TPTP in the solvent mixture yields essentially the same ignition temperature as observed with the TMMP-based mixture, with a similar volumetric component (25%) of the total solvent vapor (Figure 29).

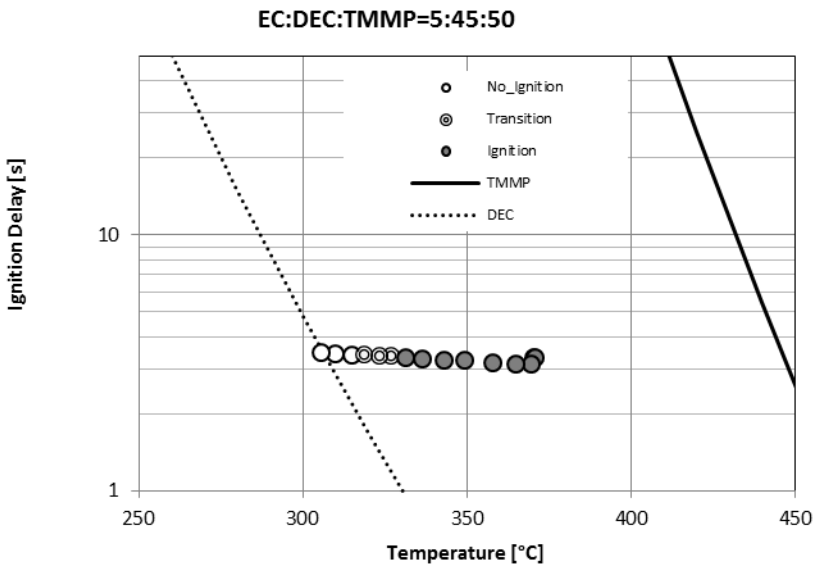

Figure 28. Measured ignition delays for fuel-rich mixtures of 5:45:50 solutions of EC, DEC and TMMP in air.

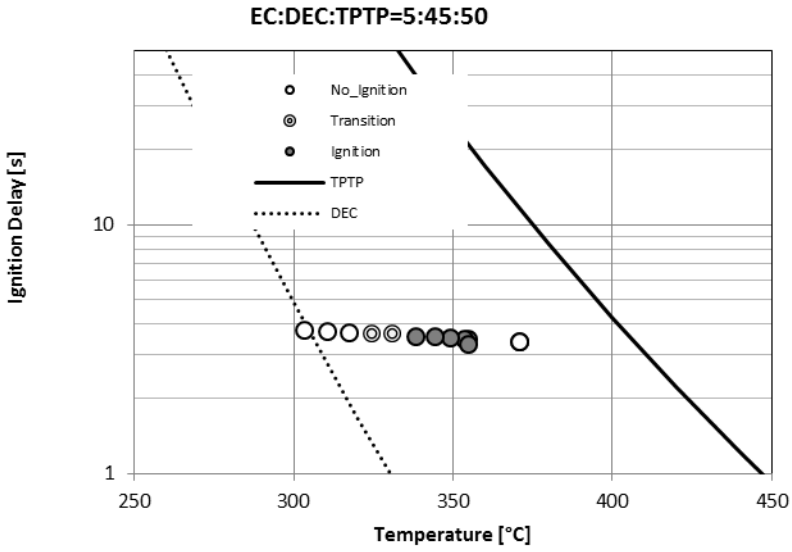

Figure 29. Measured ignition delays for fuel-rich mixtures of 5:45:50 solutions of EC, DEC and TPTP in air.

2.7. Summary of results

Li-ion cells are dominating the field of hand-held devices such as cell phones and computers. Due to their widespread success, the application space is expanding to include transportation, utility grid scale energy storage, space system, and military applications. Although Li-ion cells have tremendous potential, the flammability of the organic electrolyte hinders its consideration for large scale applications where the battery is expected to operate over a wide temperature range and the ramifications of a safety event are of major consequence. Since safety cannot be compromised, well thought out and judicious approaches have been implemented to combat flammability with varied success. FR additives seem to improve the thermal stability of the electrolytes but none seem to perform adequately. Ionic liquids have been tried as electrolytes since they are nonflammable but their higher viscosity and lower ionic conductivity is detrimental to low temperature performance. While performing adequately under thermal abuse conditions, the jury is still out on the ability of these electrolytes to remain nonflammable as the cell ages. We have shown that the electrolytes containing HFE are nonflammable, produce less gas and the onset of gas evolution is pushed out in temperature by ~80 ºC compared to the baseline. Full cell thermal ramp test shows that TMMP cell is flammable and TPTP is not. Both these showed nonflammability when tested by themselves but in full cell the TMMP is flammable. However, TPTP electrolyte is nonflammable even in full cell. More rigorous testing should be done to see if these observations are reproducible.

We have shown that the electrolytes containing HFE are nonflammable, produce less gas and the onset of gas evolution is pushed out in temperature by ~80 ºC compared to the baseline. Full cell thermal ramp test confirm that TPTP containing electrolytes are nonflammable in cells. Results for TMMP cells were somewhat convoluted by separator failure and cell shorting, but did self-ignite and burn in this case. Results highlight the importance for testing electrolyte flammability in cells and under cell-like conditions and (inadvertently) demonstrates one of the key failure modes associated with poly(olefin) separators. Auto-ignition measurements show greater resistance to ignition by the HFE solvents than carbonate solvents when measured at ambient pressure.

3. ADVANCED SEPARATOR MATERIALS

3.1. Separator Abuse Tolerance and Battery Failure

Many of the multilayer poly(olefin) separators are designed with a shutdown feature, where two of the layers have different phase transition temperatures. As the temperature of a cell increases, the lower melting component melts and fills the pores of the other solid layer and stops ion transport and current flow in the cell [9]. It is important to note that most shutdown separators were first designed for the consumer market, which are generally low voltage (<20 V), smaller battery systems (<10 A). If applied to higher voltage, larger battery systems, the abuse tolerance and shutdown function may or may not be as robust. All test results will be dependent on material choice, manufacturer, quality, design, etc. Figure 30 shows two examples of overcharge test results for cells with shutdown separators with that highlight the potential weaknesses in using poly(olefin) separators. In Figure 30a, a lithium nickel cobalt aluminum oxide (NCA) cell is overcharged at a 1C rate. The cell can temperature increases to 125 °C at 170%SOC (approx. 135 °C internal temperature) and the separator shuts down, but in this case the compliance voltage limit was set to 20 V. At this limit, the cell continues to draw current which develops into an internal short circuit and thermal runaway. This is consistent with observations made by Roth et al. for shutdown separators under overcharge abuse testing [21]. Figure 30b shows a $LiCoO_2$ cell that is overcharged at a 2C rate. In this example, when the cell temperature reaches the separator shrinkage temperature (110 °C), the cell shorts internally and goes into thermal runaway. Overcharge abuse tolerance of shutdown separators is highly dependent on the test conditions, where modest changes in the voltage limits or charge rates can have a profound impact on the separator performance and the test results. It should also be noted that the failures in these two examples occurs at temperatures well below the runaway temperatures for $LiCoO_2$ (180 °C) and NCA (190 °C), suggesting that separator failure may contribute to premature cell failure under certain abuse scenarios. These results are consistent with results described in the literature where shutdown separators can continue to pass up to 200 mA at 20 VDC and 350 mA at 30 VDC, which can quickly develop into an internal short circuit and cell runaway [21]. While this might be a low probability event, the consequences could be quite severe. This type of abuse and cell failure are unique to larger, higher voltage batteries that may not have been anticipated or designed for in scaling up from low voltage consumer electronics scale batteries, highlighting the importance of selecting the correct cell components for the application.

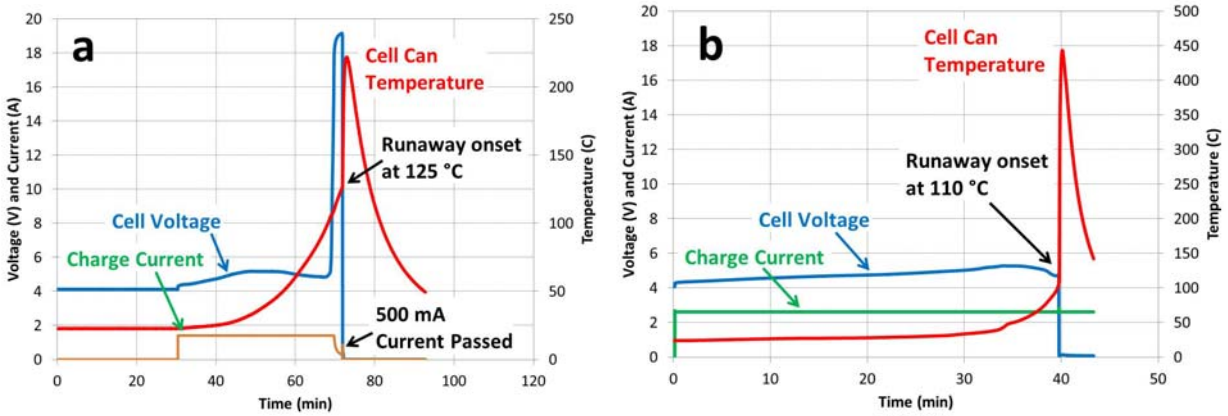

Figure 30. Overcharge abuse test of (a) NCA and (b) $LiCoO_2$ 18650 cells showing cell failure coinciding with the separator shutdown and shrinkage temperatures, respectively.

There are two general approaches to resolving these potential instabilities with lithium-ion cell separators. For low-voltage applications, one strategy is to develop separators with much lower shutdown temperatures (< 80 °C), well below the onset of catalytic reactions that can lead to thermal runaway and reducing probability of a high consequence failure. This may be an attractive approach for low voltage batteries (<12 V) where possible stand-off voltages will not be high enough to pass leakage current through the shutdown separator, but may not be a suitable option for higher voltage batteries. Another strategy is to improve the thermal stability of the separator (and all components) to close the gap between the separator shrinkage/shutdown/degradation temperature (110/135/165 °C) and the cell runaway temperatures, in general > 200 °C, depending on cell chemistry [69]. This approach would eliminate any potential lower temperature separator instabilities that could lead to internal shorting and runaway. There are advantages and trade-offs to both strategies depending on the application and these are the areas of active research in the battery safety community. This focus of this work is on the latter approach where the thermal stability of separators is improved to close the gap between separator softening/degradation temperatures and cell runaway temperatures. Figure 31 shows heat flow measurements by DSC for several poly(olefin) separators with melting temperatures between 135 and 165 °C along with an alternative, higher melting temperature poly(ester) separator. In addition to conventional stand-alone sheet material separators, we have also investigated the utility of castable separators and other unique processing approaches to making high temperature stable separators for lithium-ion batteries.

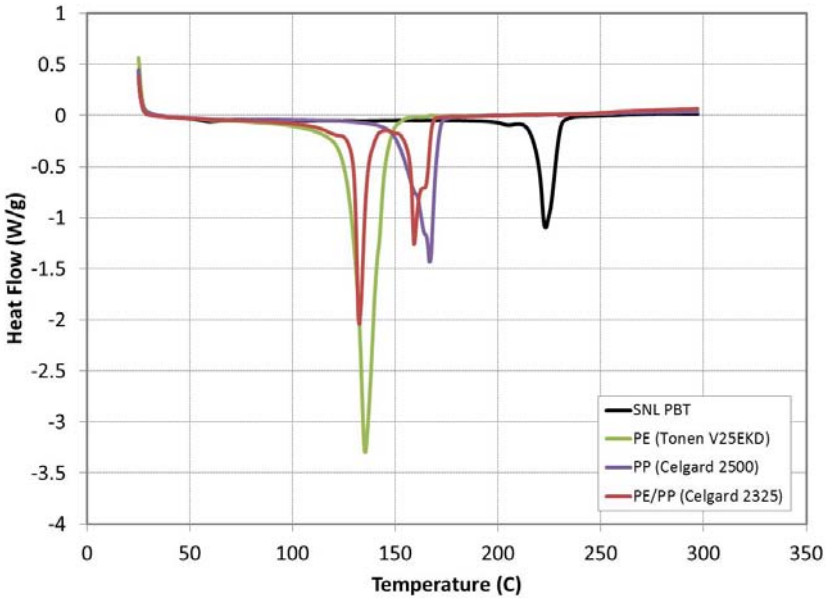

Figure 31. Heat flow (W/g) as a function of temperature (°C) measured by DSC for a series of separators: SNL PBT (black trace), PE (green trace), PP (blue trace), and multilayer PE/PP (red trace).

3.2. Poly(ester) separators for lithium-ion batteries

3.2.1. Poly(ester) separator processing

Poly(butylene) terephthalate (PBT) and other analogous poly(esters) were processed into separator films by a room temperature electro-spinning process. The structure of PBT is shown in Figure 32, as an example. Typically, PBT polymer solutions were prepared by dissolving the polymer in 1:1 (v:v) trifluoroacetic acid (TFA): methylene chloride (CH_2Cl_2) at either 5 or 10 weight % followed by bath sonication for a minimum of 30 minutes prior to electro-spinning.

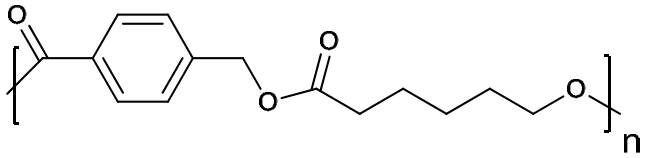

Figure 32. Chemical structure of poly(butylene) terephthalate (PBT).

The electro-spinning apparatus consisted of a needle (15 or 20 gauge), a ground electrode (aluminum or nickel foil collector plate ~ 100 cm^2) and high voltage power supply (0-20 kV, Spellman High Voltage Electronics Corporation) power supply. The power supply was connected to the needle with working voltages typically between ~ 11-17 kV and the polymers were electro-spun at working distances of either 10 or 15 cm in an inverted format. Polymer

solution flow rates were controlled with a syringe pump apparatus (Bioanalytical Systems Inc.) and ranged from 0.72 mL/h to 1.44 mL/h. All electro-spun polymers were collected under ambient temperature and humidity.

This electro-spinning process has also been scaled up to ~ 1500 cm^2 for single 18650 cell builds. A similar apparatus was used with the exception that a rotating nickel foil belt was used for the collection plate and the polymer was electrospun horizontally (Figure 33). The polymers were electro-spun until "complete" coverage of the nickel foil was obtained and then processed as follows.PBT/ or (other poly(ester))/nickel collector plate samples were dried in vacuo or in air and then mechanically pressed (Carver, Hydraulic Unit Model #3912) between two stainless steel plates, typically at 500-2000 psi and ambient-200 °C. The pressed polymer films were removed from the nickel collector plate (with careful peeling assisted with ethanol wetting as needed) and allowed to air dry before further analysis or assembly into coin (2032) or 18650 cells. Thickness of the membranes was measured using a micrometer (Mitutoyo, IP65) before and after removal from the foil.

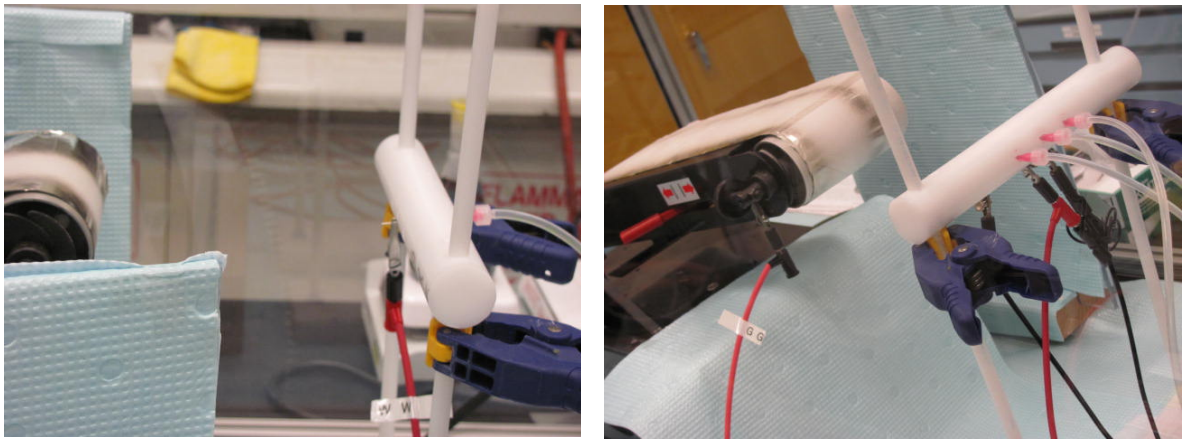

Figure 33. Images of electro-spinning apparatus used to collect 4" x 36" elecrospun mats for use in 18650 cells.

3.2.2. Poly(ester) separator properties

Non-woven mats are common separator formats for aqueous batteries because they are generally low cost, easy to process, and are scalable to roll-to-roll manufacturing, and have even drawn some attention for use in lithium-ion cells [70-73]. The technique of electro-spinning polymers into mat sheets has long been a laboratory scale technique, but has recently been scaled in commercial equipment for large scale manufacturing processing, making it a viable approach for the production of separators for lithium-ion cells. While most thermoplastics, like PBT, are electro-spun at high temperature, we have developed a technique for electro-spinning PBT at ambient temperature from solution, as described above. Under these preparation conditions, the resulting electro-spun polymer films are fiber mats made up of polymer fibers that are ~200-500 nm in diameter; the target fiber diameter to match the RMS roughness of a lithium-ion cell

positive or negative electrode. The as-prepared films are heat pressed to improve their mechanical stability and film uniformity and have pores that are ~1 μm in diameter (Figure 34). Figure 34b also shows that these development PBT separators are nominally 55 μm thick in the cross-section image which is approximately twice the thickness of conventional separators (25 μm). However, processing improvements have been made to reduce the thickness of these development PBT separators to 30 μm or less, shown in Figure 34c. This report will focus on the performance and thermal stability of these 55 μm thick separators. The average porosity of these separators is 75% (calculated using a PBT density of 1.31 g/cm^3), which is consistent with the high porosities (up to 65 %) reported for other non-woven separators [73]. It is interesting to note that this high degree of porosity makes these separators extremely permeable. The Gurley numbers for these separators, measured by air permeability through a 1 in^2 area, are 6 ± 1 s/100 mL; which is as much as two orders of magnitude faster (more permeable) than that published for commercial extruded separators (Table 8).[9,10] Ambient temperature ionic conductivity of these PBT separators (0.27 mS/cm) is slightly less than that of commercial separators (0.41 mS/cm). While there is limited information available in the literature on ionic conductivity of fiber separator membranes, the conductivity of the PBT membranes is an order of magnitude greater than that reported by Song et al. for the PMMA/ PVDF composite gel membranes (10^{-2} mS/cm) [70].

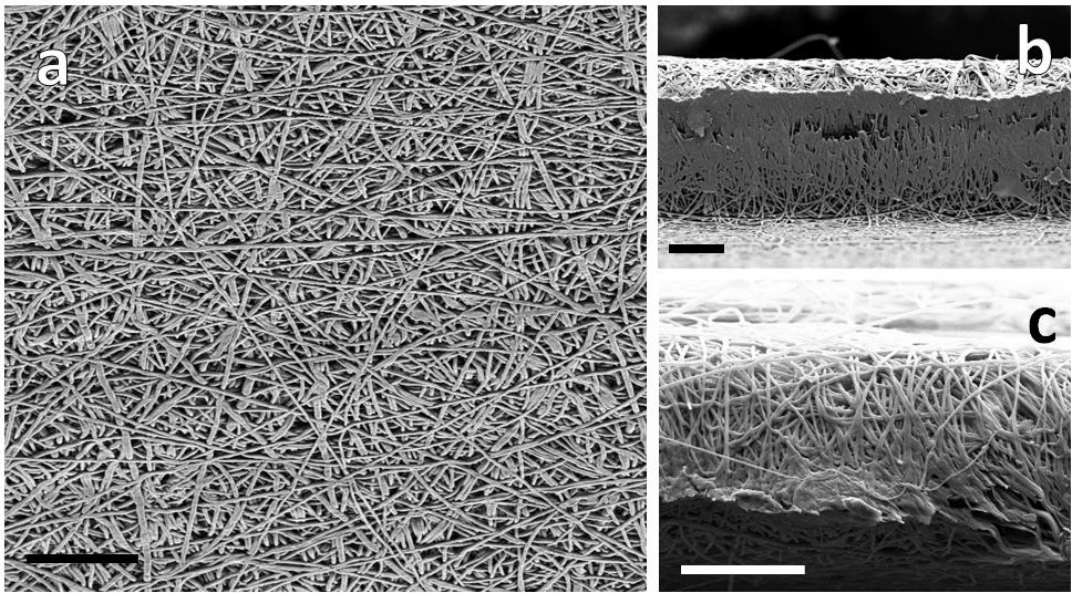

Figure 34. SEM images of PBT separartors showing in both the (a) top-down, and (b and C) cross-section views. Scale bar represents 20 μm.

Table 8. Physical characteristics of commercial and development separators.

Separator	(μm)	Gurley (s/100 mL)		Ionic Conductivity (mS/cm)
		Measured	Reported[a]	
Celgard 2325	25	570 ± 4	620[a]	NM
Celgard 2400	25	NM	620[a]	0.41[b]
Celgard 2500	25	231 ± 4	200[a]	NM
Tonen 25MMS	25	637 ± 10	650[a]	NM
Tonen 20MMS	20	524 ± 9	540[a]	NM
Tonen V25EKD	25	NM	270[a]	0.41
SNL PBT	55	6 ± 1	NA	0.27

[a]Reported Gurley numbers from the manufacturers specification sheets for these products
[b]from Reference 17.
NM – no measurements made for this separator

3.2.3. Poly(ester) separator performance

The performance of these PBT development separators was evaluated against a commercially available separator (25 μm thickness). 2032 coin cells with NMC/Graphite/1.2 M $LiPF_6$ EC:EMC (3:7) (no additives), prepared in our laboratory, are used to compare relative discharge capacity, capacity retention, and rate capability. The objective of this work is to demonstrate baseline functionality of the PBT separators as compared to commercially available separator material. Figure 35 shows the discharge capacity for 50 charge-discharge (C/D) cycles of cells with commercial PE separator (Tonen V25EKD) and a representative SNL PBT separator. The commercial PE and SNL PBT cells have identical discharge capacities over the course of these measurements. Both cells show 8% capacity fade over the 50 C/D cycles with no observable differences in fade between the commercial and PBT development separators. The rate capability of these PBT separators is measured from C/10 to 3C and the discharge capacities for each cycle are shown in Figure 36. At all discharge rates measured, the capacity for both the SNL PBT and commercial PE cells are very comparable; ~150-160 mAh/g at C/10 and C/5, ~140 mAh/g at C/2, ~90 mAh/g at 1C, ~20 mAh/g at 2C. It is important to note that the PBT development separators have comparable discharge rate performance in spite of the fact that they are more than twice as thick as the Tonen PE separator. This is consistent with the fact that these development PBT films have greater porosity and permeability than the commercial polyolefin separators. Long term aging and life cycling are important in understanding how these PBT separators behave over time, however, were not studied as part of this project.

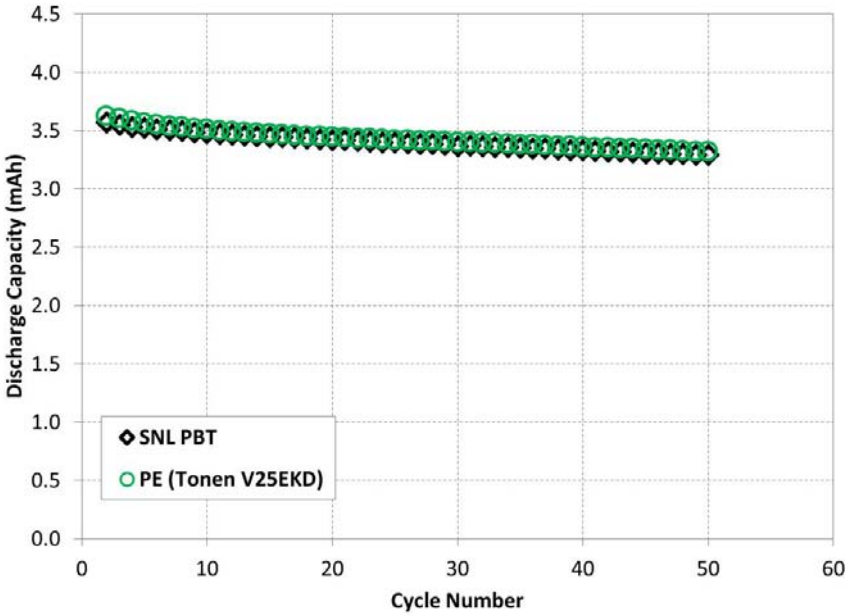

Figure 35. Full cell discharge capacity at C/15 of NMC/Graphite cells in 1.2 M $LiPF_6$ in EC:EMC (3:7) with SNL PBT separator (black symbol) and commercial PE separator (Tonen) (green symbol).

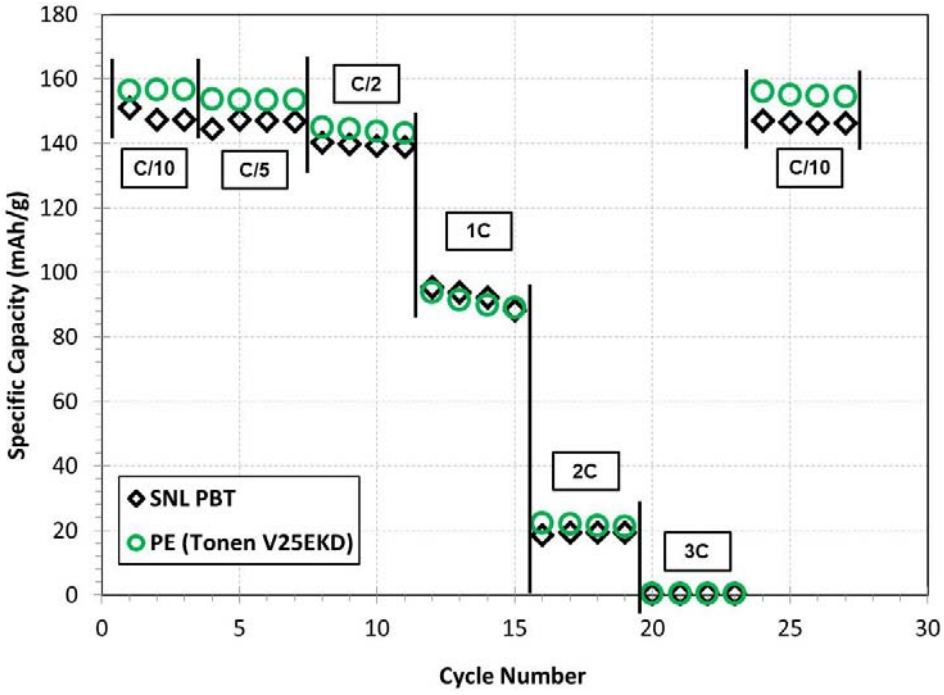

Figure 36. Discharge capacity as a function of cycle number at C/10, C/5, C/2, 1C, 2C and 3C rates for NMC/Graphite cells in 1.2 M $LiPF_6$ in EC:EMC (3:7) with SNL PBT (black symbol) and commercial PE (Tonen) (green symbol) separators

One concern with using new materials for lithium-ion cells is the electrochemical stability and potential chemical reactivity of these polyesters in the extreme environment of a lithium-ion cell. Raman spectroscopy is used to evaluate the chemical integrity of these PBT materials in cells. Figure 37 shows the Raman spectra for bulk PBT, as-prepared SNL PBT separator, and SNL PBT separator harvested from cells that were cycle aged (50 cycles) at C/10. The vibrational peak frequencies and assignments are shown in Table 9. As-received PBT shows characteristic Raman vibrations modes corresponding to symmetric and antisymmetric methylene stretching ($\nu_s(CH_2)$ and $\nu_a(CH_2)$) at 3082 and 2940 cm^{-1}, respectively, symmetric carbonyl stretching ($\nu(C=O)$) of the ester carbonyl at 1715 cm^{-1}, ring breathing modes ($\nu(C=C)_{ring}$) at 1615 cm^{-1}, carbon stretching at 1282 and 1106 cm^{-1}, and C-H bending and deformation at 859 cm^{-1} [74-76]. Electro-spinning PBT to make separator sheets has no observable impact on the chemical nature or structure of the material in the Raman spectroscopy; peak frequency shifts and relative ratios are comparable to the bulk, as–received PBT. Likewise, PBT separators harvested from cycled lithium-ion cells show no observable chemical differences nor any new reacted chemical species (electrochemical reduction of alkanes moieties to alkenes, electrolyte or lithium reaction products) from the as-received PBT separator or bulk PBT. This suggests that PBT is a viable candidate material, compatible with conventional lithium-ion cell materials and electrochemical cell potentials (evaluated up to 4.3 V). However, these observations are made on a particular electrochemical couple/electrolyte system and for a limited number of cycles.

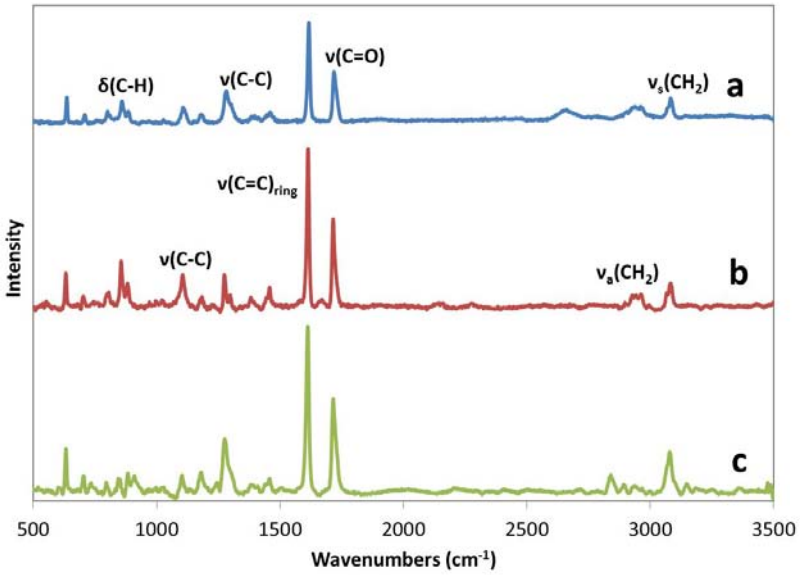

Figure 37. Raman spectra of (a) bulk poly(butylene terephthalate) (PBT), (b) as-prepared SNL PBT separator sheet, and (c) SNL PBT separator removed from a lithium-ion cell that was aged 50 cycles at C/10.

Table 9. Raman peak frequencies (cm^{-1}) and assignments for PBT separators.

PBT (bulk)	As-prepared PBT separator	Cycle-aged PBT separator	Assignment[a]
3082	3081	3080	$\nu_s(CH_2)$
2940	2940	2944	$\nu_a(CH_2)$
1718	1715	1715	$\nu(C=O)$
1615	1612	1613	$\nu(C=C)_{ring}$
1282	1272	1275	$\nu(C-C)$
1106	1105	1104	$\nu(C-C)$
859	856	855	$\delta(C-H)$

ν = stretch, δ = deformation

[a]From References [75-77]

Separator thermal stability is studied by measuring separator impedance at 1 kHz (50 mV AC) with increasing temperature. These measurements are made under battery-like conditions as described previously [21, 78]. Briefly, separator samples (approx. 1 in^2) are soaked in high temperature electrolyte (1 M LiTFSI in 1:1 PC:triglyme) at ambient temperature and pressure for >30 min prior to sample preparation. Soaked samples are sandwiched between two stainless steel electrodes and sealed in polyimide tape (to minimize exposure to moisture and to maintain structural integrity of the sample). Samples are heated at 5 °C/min to either 250 °C or until the impedance approaches zero. Samples are measured under a constant 5 psi load while monitoring impedance at 1000 Hz. Figure 38 shows normalized separator total impedance (Z_{total}/Z_0) as a function of temperature for PBT commercial separators. Because of some scatter in the initial impedance values for each sample ($10 < Z_0 < 60$), total impedance data are normalized to the initial impedance value (Z_{total}/Z_0) for each sample to put all of the data on the same scale. For all samples, the impedance decreases with increasing temperature to 110 °C. At 110 °C, Commercial PE (Tonen) shuts down and the impedance increases by five orders of magnitude (off scale in Figure 38). Celgard PP and multilayer PE/PP separators shutdown at 140 and 130 °C, respectively. Between 160 and 170 °C, the commercial separators completely melt, degrade, and the total normalized impedance approaches zero, consistent with results for commercial materials reported by Roth et al.[21] It is important to note that the normalized impedance of the commercial PE (Tonen) does not reach zero, suggesting some improved mechanical stability at high temperature compared to the other commercial materials.[21] For the PBT separator, there is an inflection in the impedance vs. temperature data between 110 and 120 °C where the impedance increases slightly. In the temperature range from 135 to 165 °C, the PBT separator impedance continues to decrease with increase temperature and no phase transition, shutdown, or degradation are observed. At 210 °C, PBT melts and the normalized impedance drops off and approaches zero; consistent with the melting point of the polymer (Figure 38). These results suggest that PBT separators are thermally stable under these experimental conditions to > 200 °C and close the gap between the separator phase transition and the runaway temperatures of lithium-ion cells. This improvement in thermal stability may offer some improvement in abuse tolerance for lithium-ion cells.

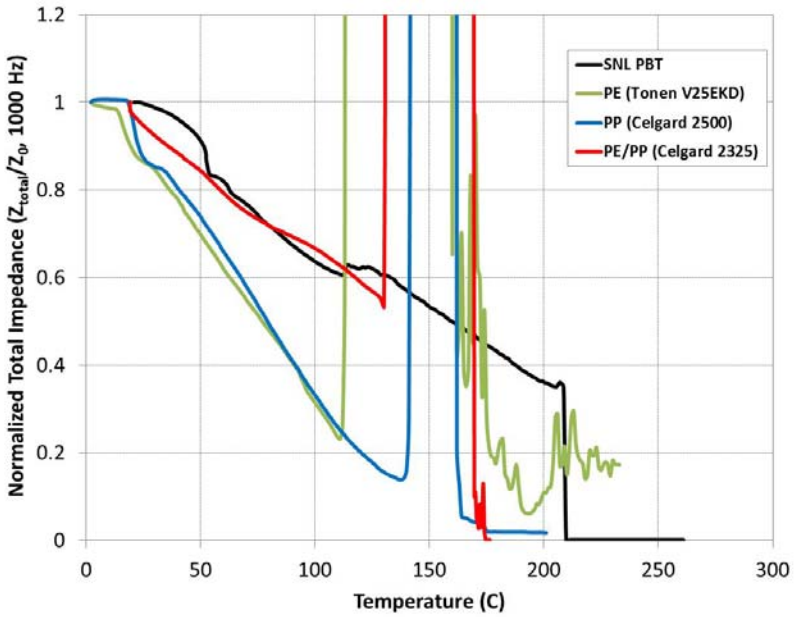

Figure 38. Normalized separator AC impedance (Z_{total}/Z_0, 1000 Hz) as a function of temperature for SNL PBT separator (black trace), PE separator (green trace), PP (blue trace), and multilayer PE/PP separator (red trace).

3.3. Direct coat, castable separators for lithium-ion batteries

Since most of the very high temperature insulators are ceramics with melting points significantly in excess of the working temperatures of every other component in the battery, the only reasonable way to incorporate these kinds of materials is by working with them either as dry powders or as slurries in a solvent. Dry powder work would be incompatible with some of the forces encountered when assembling and cycling a battery, but slurries of ceramics could be incorporated into the battery if a means could be found to produce a bound, stable, porous matrix of ceramic bound into a separator layer.

To make such a coating, a combination of solid ceramic phase ("scaffold"), soluble polymeric phase ("binder"), and solvent need to be made in such a way so that the resulting structure. Once the solvent has been removed through drying, has good adhesion to the surface it is applied to (usually either the anode or cathode layer of the battery), as well as good cohesion to itself, minimizing cracking and spalling of the film. It should also be relatively porous, which argues for a relatively high liquid content in the mixture (low solids content), but at the same time, the mixture, while in the solvated state, should be rheologically pseudoplastic to allow for easy coating, which argues for a higher solids content. Add to this that the solvent should not interact (or redissolve) the layer it is being coated over, and a relatively small number of perturbations on these combinations becomes available.

The initial material chosen for evaluation as ceramic separators with polymeric binders was alumina. The wide availability and low cost of this material makes it an ideal candidate for separator production. Since the ceramic is stabile to much higher temperatures than any other

battery component, the binder used to immobilize the alumina would be the primary contributor to the thermal stability of the separator.

Previous work on binders has shown that a variant of tetraethylorthosilicate (TEOS), in which not all the Silicon coordinating ligands are ethyl groups, but have some methyl groups (n-methyl-n-ethylorthosilicate) provides a more open structure, and meets many of the above criterion for a binder. It solubilizes readily into dimethylbenzene and other aromatic solvents, but not into alcohols or pyrrolidones, which are used in the creation of the anode and cathode layers of the battery. This binder was used with tabular alumina (Almatis T60/T64) at a mixture ratio from 5-10 wt% binder and 35-43 wt% alumina, with balance xylene solvent. The mixtures varied in rheological behavior between ~1cP to 200cP. They were cast onto stainless steel, and dried at 160 °C for 30 minutes in a vacuum oven, followed by 4 hours at 200 °C in air for crosslinking, followed by 250 °C for 2 hours to fully densify the binder. A final step of 290 °C for 16 hours in an argon environment was used to finish the reaction of the binder and drive off any remaining unreacted materials. Scanning electron microscopy (SEM) images of the resulting coatings were made, and uniformly showed a very dense film with little overall porosity (Figure 39). Since there was relatively little binder in this mixture to begin with, the observed low porosity is simply due to the shape and size distribution of the particles.

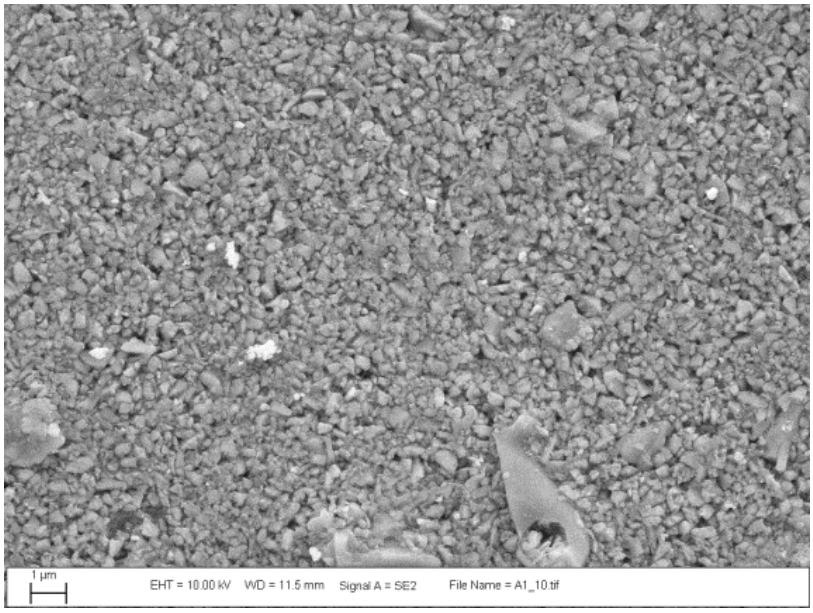

Figure 39. 10% binder on tabular alumina, low porosity. Scale bar represents 1 µm.

After slurry optimization for direct coating onto an electrode it was found that a binder to ceramic ratio of 5:95 wt% produced the most uniform and reproducible separators. Using a 2 mil doctor blade, ceramic separators were coated on both premade NMC 111 cathodes (94 wt% active material) and intercalation carbon anodes (92 wt% active material) as seen in Figure 40. All samples were annealed at 200 °C to densify the separator. Fabrication of 2032 coin cells using the directly coated cathode separators proved difficult due to fracturing and delamination of the ceramic phase from the cathode. This was less of an issue using the directly coated anode separators.

Figure 40. Ceramic separator cast directly onto cell electrodes.

Five different alumina materials were evaluated for use as a direct coated separator. Three of the alumina materials (A15 SG, Aeropal 400, and AKP 53) produced films that were too brittle to retain their form when assembled into a cell, causing a short circuit within the cell. The samples made using A3500 SG alumina and T64 tabular alumina were able to complete formation cycling using the NMC 111 cathodes versus the carbon anode.

The A3500 SG separator had the best adhesion to the anode out of any of the materials tested. The film did not crack during punching operations or cell assembly, which was the main failure mode for the alumina materials unable to be fully cycled. Formation cycles and capacity can be seen in Figure 41. At the end of the five formation cycles the capacity was 0.7 mAh, which is substantially lower than the expected value of 1.90 mAh based upon the electrode loading of 6.62 mg cm^{-2} and the theoretical capacity of the NMC material.

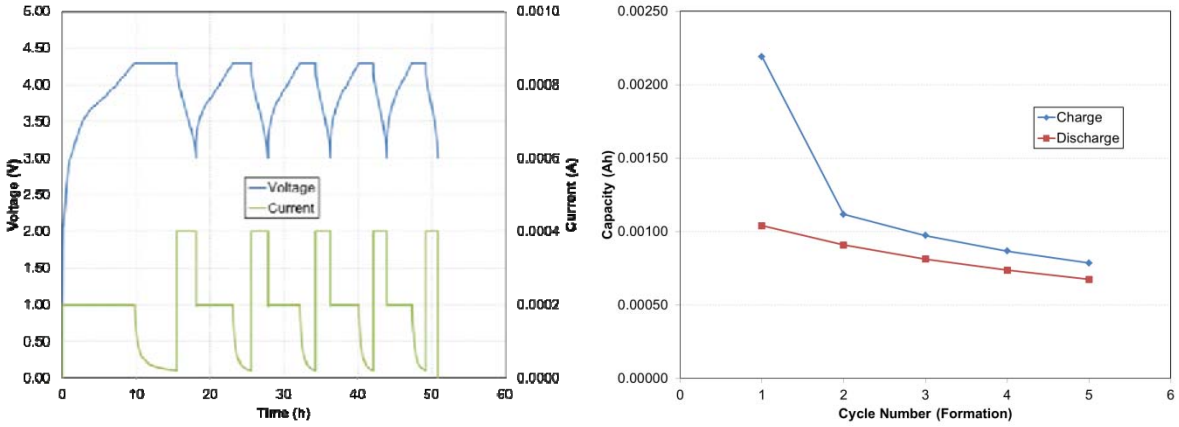

Figure 41. Formation cycling for A3500 SG alumina separator.

The tabular T64 alumina showed good behavior and good capacity after formation cycling, as shown in Figure 42. The final capacity for the T64 alumina after formation cycling was 1.6 mAh, which is very close to the theoretically expected 1.9 mAh.

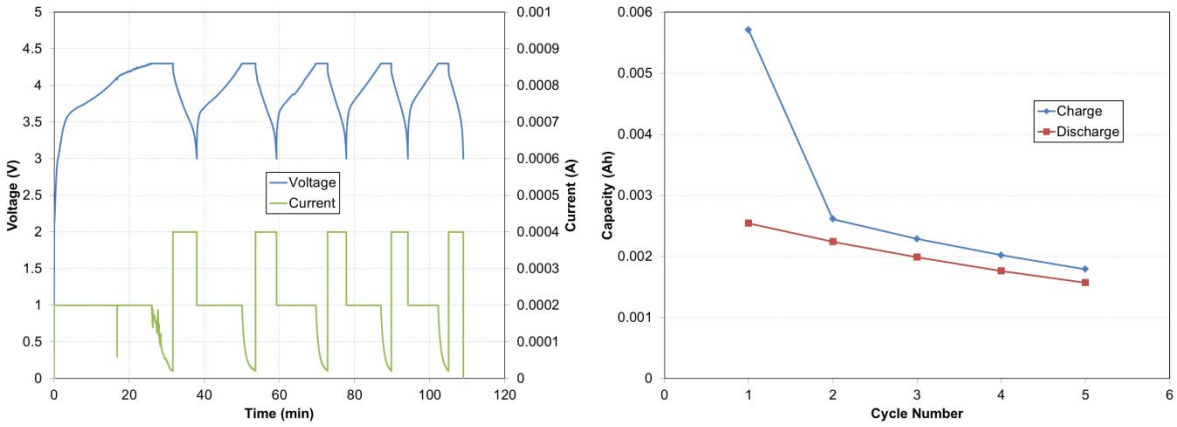

Figure 42. Tabular T64 direct coated separator formation cycling.

The primary difference in all of the tested materials is the microstructure created during the coating process. SEM images taken of the T64 alumina (the best electrochemical performing separator) and the AKP 53 (the film with the most uniform coating and best adhesion to the electrode) show that the T64 separators have an open pore network formation and the AKP 53 have a very tightly packed network with very little porosity, as shown in Figure 43. The inverse relationship between electrochemical performance and rheological properties for these alumina based separators hinders their application in cells.

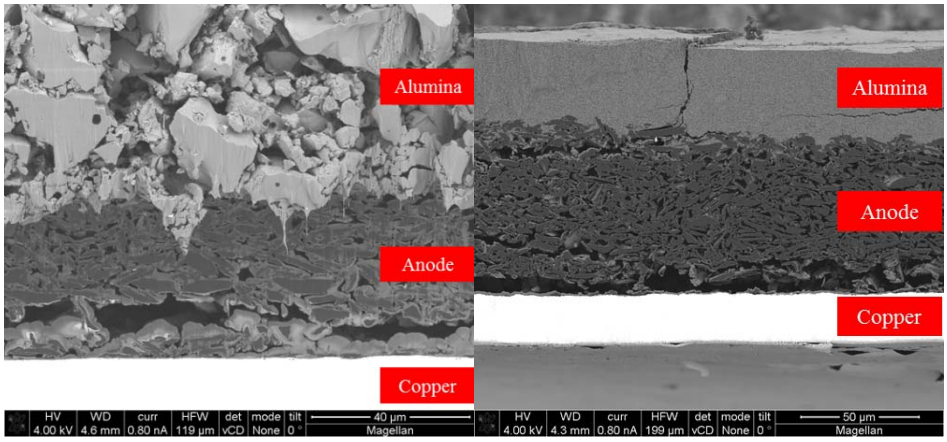

Figure 43. SEM cross-sections of T64 tabular alumina (left) and AKP53 alumina (right) separator coated directly onto the anode.

To try to increase the porosity of the cast film while maintaining rheological properties, a much higher aspect ratio particle, in the form of zirconia (ZrO_2) rods, was chosen to replace the alumina. Using the ratio by mass for the mixture (5% binder, 40% ZrO_2, 55% xylene) resulted in a mixture that was almost completely dry; the ZrO_2 powder completely absorbed both the xylene and the binder. Increasing the solvent up to an equivalent of 90% solvent allowed the material to go into solution, although the resulting films were not stable, and would rub off the surface of the

stainless steel quickly after drying. Increasing binder content is the normal response for fixing poor adhesion and cohesion, but did not work as expected for this ceramic filler. Ratios from 5% up to 50% by volume binders were prepared, and even the 50% binder remained poorly adhered to the substrate. SEM images of the coated films showed that the resulting coating was more porous than in the case of tabular alumina, the binder (which reduces to silica upon processing) was not readily observable in the micrographs (Figure 44). This may have been due to the high porosity of the zirconia filaments, or due to a loss mechanism of the binder precursor during processing. Regardless, the binder used previously would not work for these scaffold powders, and a different binder needed to be identified.

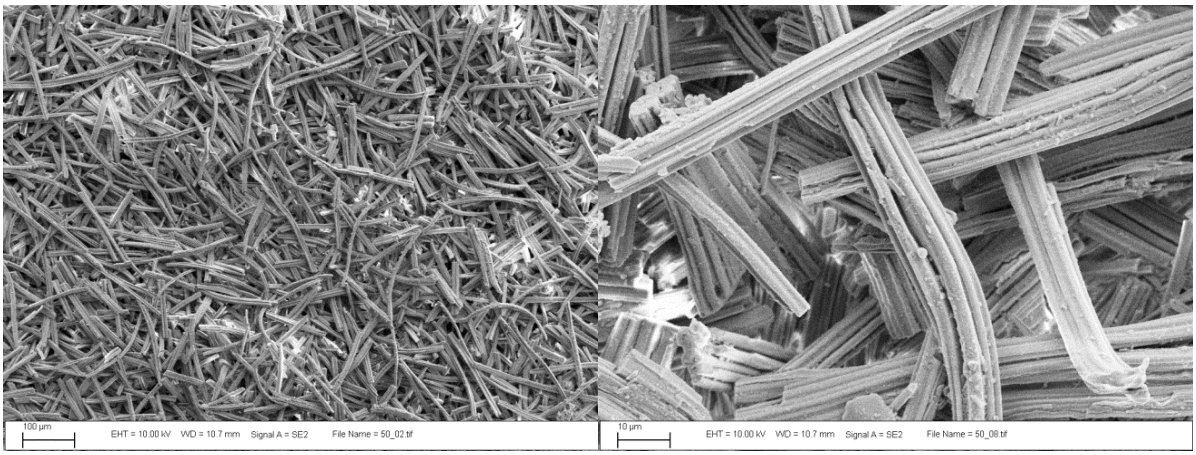

Figure 44. Low magnification (left) and high magnification (right) SEM images of zirconia fiber bound by 50 v% TEOS derivatized binder. The binder is not visible in the preparation. These films had very poor mechanical adhesion and cohesion.

3.4. Alternative binders for castable separators

Because the starting silica based high temperature binder would not produce highly porous films, a new binder system based on polymeric structures was developed. The initial path was to provide some means to hold the zirconia thread scaffold together into a stable mat for casting or spraying, and then stabilize the mat to high temperature either by dissolving off the binder agent or by condensing the binders. In this way, a high temperature, castable “glass mat” separator could be realized that would provide the ease of processing of casting with the high temperature resistance of traditional glass mat separators currently in use in other battery systems. The most used binder is polyvinylidene difluoride (PVDF), which can be solubilized into several solvents, most notably N-methyl pyrrolidone (NMP), but will not solubilize into battery electrolyte solvents. PVDF melts at relatively low temperature, however (~177 °C). While PVDF is also used to bind anode and cathode, and so NMP is not an optimal choice for the separator binder due to possible resolubilization of the active layers, the content was intended to be low, as the majority of the separator was to be the zirconia thread. Initial tests with this binder/scaffold mixture also resulted in films with very poor adhesion and cohesion, unless unacceptably large volumes of binder were used, which would be difficult to remove or stabilize after casting, and

would reduce the porosity of the cast separator. Instead, efforts were made to work with a binder alone that would be able to survive processing at elevated temperature, which would obviate the need for post processing after casting the separator or running the risk of having the separator melt at a low temperature.

Table 10 shows the array of high temperature, electrochemically stable polymers for binders that could be considered for this application, along with their maximum use temperature, their glass transition temperature, and the most common methods for manufacture of the material. Method of manufacture is important due to the need to be able to solubilize these materials and recast them onto the ceramic scaffold as a binder, or to prepare them in such a way that they themselves could be made as the separator by being able to process pores into the polymer film.

Table 10. High temperature polymers, listed with use and softening temperatures, and main methods of processing.

Polymer	Use (°C)	T_g (°C)	Manufacture
Polytetrafluoroethylene	260	327	extrusion from melt
Polyaryletherketone	120	143	extrusion from melt
Perfluoroalkoxy resin	260	316	extrusion from melt
Polyether Imide	170	216	casting, cure
Fluorinated Ethylene Propylene	204	260	casting, cure
Poly(p-xylylene) (parylene AF-4)	350	burns	gas phase deposition

Polytetrafluoroethylene (PTFE, Teflon™) Is currently used in batteries (though not as a separator) and has a very good use temperature, but processing of the polymer is difficult; it does not readily dissolve into many solvents, and is relatively difficult to cold work. Polyaryletherketone (PEEK) has a very low use temperature, and is a brittle, semicrystalline polymer. Polyfluoroalkoxy resin (PFA) has a high use temperature, and can be made into thin sheets, but is, like PTFE, difficult to solubilize and work in casting systems; it also has only marginal stability at low potentials, making it unsuitable for use in batteries. Polyether Imide (PEI) and Fluorinated Ethylene Propylene (FEP) can be cast, and are cured from a reactive mixture. But both of these materials have bonds that will not be stable within the voltage window of batteries, and so are unsuitable for the same reason as PFA. Poly(p-xylylene), better known as parylene, has an extremely high use temperature, and is a thermosetting polymer, rather than a thermoplastic. It also has an interesting method of deposition; the monomers are evaporated into the gas phase, and polymerize spontaneously on adsorption onto a surface. The polymer is used extensively in the semiconductor industry to make thin, insulating, pore free films for microelectronics, and could be an excellent battery separator, but the reactivity of this polymer with the other components in the battery is unknown, and needed to be studied prior to using it as a possible gas phase deposition binder for the zirconia scaffold.

3.5. Parylene stability, temperature, and processing

The first question is whether parylene, as a deposited sample, is stable at the lithium potential, or if the polymer will be dissolved slowly over time when in contact with the anode. To test this, a sample of 25 µm thick parylene was coated onto 100 µm nickel foil, and then placed in direct contact with a small sample of lithium metal foil. The sample was held in contact through a stainless steel spring to insure intimate contact between sample and the lithium, and then the whole assembly was placed into a bath of standard battery electrolyte (ethylene carbonate (EC), ethylmethyl carbonate (EMC), 3:7 ratio, with 1.2M $LiPF_6$ salt). All mixing and preparation was done in a glove box under inert Ar, and left for several weeks. The sample was then removed periodically and inspected for signs of dissolution. Even after several months of exposure, the sample retained its initial clean coating, and no observable degradation to the parylene was observed. Parylene coatings were also tested up to 250 °C in the presence of molten lithium, and no adverse effect was observed on the coating after exposure for several weeks.

Processing of the samples was straightforward, and taken directly from the microelectronics processing; a sample of p-xylylene monomer solution was placed into a vacuum chamber along with the material to be coated, and the chamber sealed and evacuated. The temperature of deposition was roughly 55 °C. The scaffolding was prepared by creating a dry casting of the zirconia fibers, either by mixing the fibers in xylene and drop casting them onto glass slides, then allowing the mixture to dry, or by directly pressing the dry powder into an acetate film on the glass slide. The slides were placed in the parylene deposition chamber and coated to a thickness of ~15 µm. The dry casting films did not survive the pumpdown of the chamber, but the samples of zirconia fiber pressed into acetate were well coated by the parylene (Figure 45). The resulting film appeared dense and continuous. However, an unexpected issue arose in that, while the fibers were coated uniformly by the parylene, the substrate they were coated onto was also covered in parylene, and resulted in a pore free region of the zirconia fiber containing region that was closest to the acetate. This pore free region arose due to parylene deposition on the acetate itself, and would have blocked any electrolyte transport from occurring if used in a battery. To prepare a fully porous film, the scaffold would need to be free standing and self-supporting prior to the parylene coating being initiated.

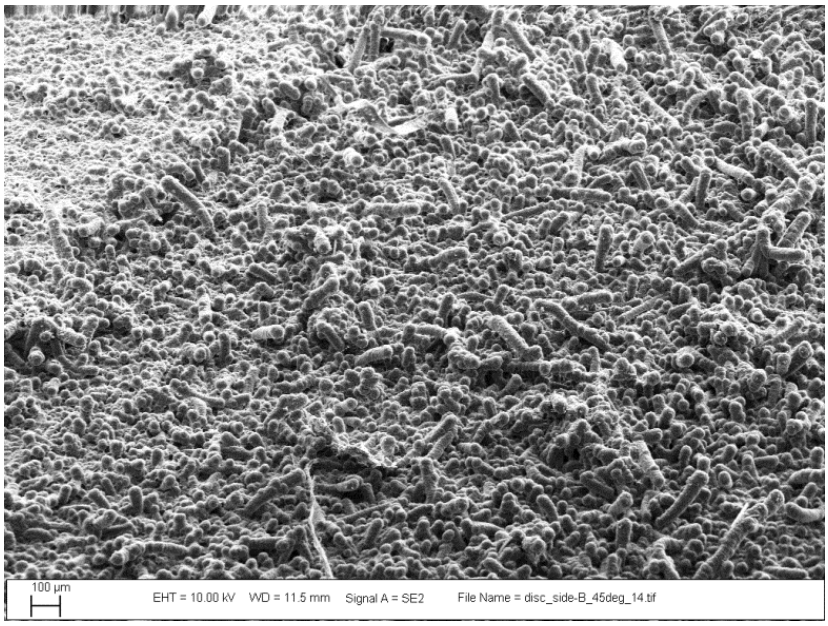

Figure 45. 15 µm parylene coating on a bed of zirconia fiber. The opposing side of the zirconia layer from the imaged side was a solid layer of parylene, resulting in a nonporous film. Scale bar represents 100 µm.

Making a porous, self-supporting structure prior to the application of parylene using the ceramics required developing a binder to hold the ceramic fibers together, which was the original intent of the development of the parylene process as it applied to making a separator. While it would be possible to use a low temperature binder (such as the PVDF outlined above) to structuralize the zirconia mat until the parylene was coated onto it, and then rely on the parylene to provide the structural integrity of the separator at high temperature, it brought to light an important consideration. The zirconia fibers were merely acting as a scaffold at this point, and providing structural porosity for the parylene, which provided the high temperature binding and chemical inertness necessary for the battery application. The requirements of the scaffold had changed from being chemically inert by itself, since the parylene would now completely cover the scaffold. With that requirement removed, a host of new materials becomes available for consideration as the structural element in the separator.

3.5.1. Paralyene separator evaluation for lithium-ion batteries

One of the easiest, and most robust, scaffolds that was considered was a metal mesh scaffolding that would allow for high porosity with straight through pores, but have sufficient structural integrity to provide isolation between anode and cathode. These meshes are commercially available in a number of different metals, alloys, weaves, and thicknesses. The thinnest available meshes were available in stainless steel or in bronze. Both of these meshes were obtained and were coated with parylene to create a separator for use in a cell.

One of the early observations with using metal mesh scaffolds was that the parylene coatings had to be much thicker than previously used in order to insure that the meshes were not electronically

conductive. Coatings of 25 µm should have been sufficient to coat the samples and achieve electrical isolation, but in these systems, it took almost 100 µm in order to guarantee that the meshes were completely electronically isolated when checked with resistance probes. It was thought that this could possibly be due to fibers or debris on the mesh that was leading to the electrical shorting behavior, but SEM images of the bronze coated mesh (Figure 46) did not show any such artifacts on the coated material. At 100 µm of parylene, however, a fully insulated mesh was achieved, and both stainless steel and bronze mesh scaffolds were assembled into coin cells and tested.

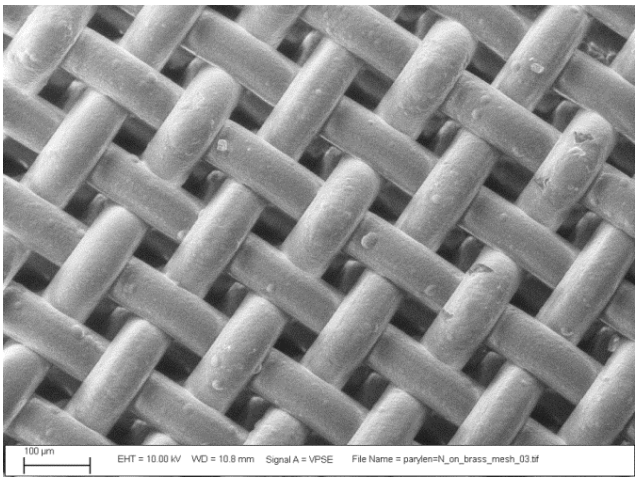

Figure 46. Bronze mesh (50 µm thick wire) after coating with 100 µm of parylene.

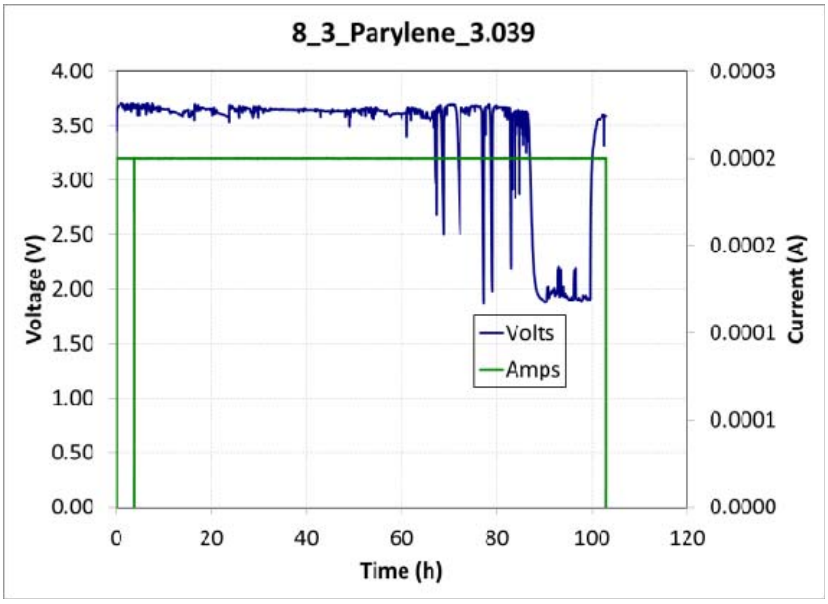

Figure 47. Half coin cell charge data for bronze scaffold separator with parylene coating. Anode: Li metal, Cathode: 523 Nickel-Manganese-Cobalt Oxide, room temperature.

The coin cell was constructed as a half cell using a 75 µm thick 523 NMC cathode, with a total capacity of around 2-3 mAh. The results of testing for the bronze mesh are shown in Figure 47. In these tests, a constant low charging current is applied to the cell, and the voltage monitored over time. When the battery is fully charged, the voltage will increase up to a limit, at which point it is held until the charging current dissipates below a threshold level. For this cell, while the initial voltage was good, holding at just over 3.6 V, the expected voltage increase was never observed. Instead, a continuous charging current existed for over 60 hours, with an accumulated charge of 12 mAh, well in excess of the known capacity for the cathode. Disassembly of the test cells showed that, although there was no electrical connection to the scaffold, there must have still been ionic contact through to it, as there was significant plating of copper on the anode of the cell. Since reduction of Cu occurs at roughly 3.6 V vs. Li, it is likely that this was the observed current and voltage of the cell, rather than a real cell voltage.

In the case of the stainless steel scaffolds, this would not be a problem, as the stainless mesh would be stable at the cathodic potential and not be susceptible to corrosion and precipitation. However, the stainless steel mesh was made from wires only 25 µm thick, and was very fragile. Punching this fragile mesh into the 19 mm disk for use in a coin cell resulted in several of the wires getting pulled and frayed from the edge of the mesh. Once these samples were coated with parylene, they were inserted into coin cells, but some of the frayed edges, although they were coated, were in contact with the gasket and casing, and it was possible, with compression, that these frayed edges were rubbed clean of the parylene coating. Testing of these cells almost always resulted in a short circuit for the cell.

Since the bronze scaffold was dissolved in the initial tests, an attempt was made to remove the scaffold from the structure before being inserted into a cell, leaving only the parylene material. Samples of the parylene coated bronze mesh were prepared, and then abraded on one side of the mesh to expose the bronze again, allowing for easy chemical access to the underlying scaffold. These samples were then placed in an aqua regia etch (3:1 nitric/hydrochloric) for 72 hours to etch out the bronze scaffold. The resulting separator, after rinsing with DI water in an ultrasonic bath and drying in a vacuum oven at 120 °C, appeared to be free of bronze scaffold, and looked like a white fabric weave (Figure 48). This separator was then punched to fit into a coin cell, assembled as described previously, and subjected to the same tests as above.

Figure 48. Parylene coated bronze mesh with the mesh dissolved, resulting in a parylene only separator.

The cell test (Figure 49) showed that the etched parylene separator was shorted from the beginning of the test, despite the fact that there was no electronically conductive material left in the separator after the aqua regia etch. Post mortem analysis of the cell showed that it was highly likely that the large pores in the parylene mesh (holes on the order of 25 µm) were sufficiently wide to allow for the cathode to distend through the pores and short to the lithium metal during assembly. This was further borne out by looking at SEM images of the separator recovered from the cell after testing (Figure 50). At the end of the program, a pouch cell was assembled that did not have the same compressive forces on the cell to extrude the cathode through the separator. The cell completed two cycles during formation, but shorted and failed after the 2nd cycle because of the same cathode extrusion issue (Figure 51). While this method may in fact yield a good separator, the pore size from the scaffold will have to be significantly reduced in order to make the material useful in a battery cell configuration.

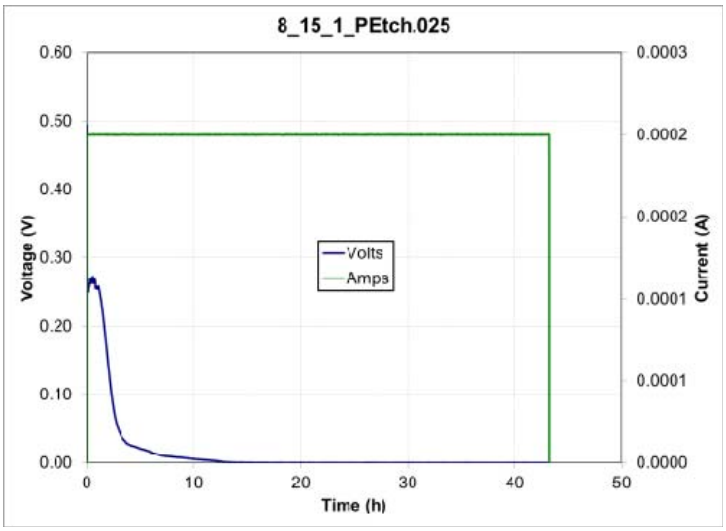

Figure 49. Charge cycle with parylene coated bronze scaffold, with the scaffold etched away. The cell has shorted from the beginning of the test.

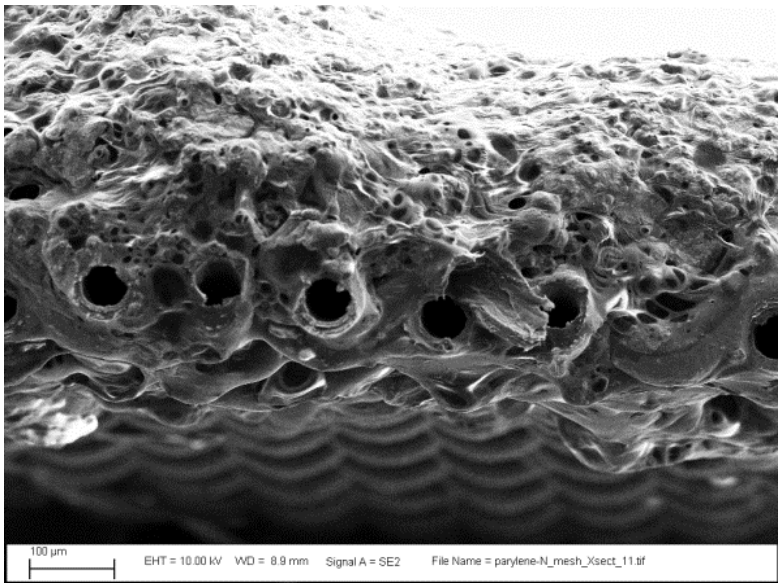

Figure 50. Parylene coated bronze scaffold subsequently etched away, leaving only parylene, then assembled into a coin cell and tested. The holes from the scaffold are visible in the center of the image. The cathode material is visible on the top of the image, and a small section of cathode is visible having extruded onto the anode side of the separator in the bottom right.

At the end of the program, two new scaffolds that were insulating to begin with and would not need to be etched had been ordered; one consisting of a ~250 µm mesh of PTFE, the other of a ~250 µm mesh of nylon. These could both be coated with parylene and tested without having to be etched, but given the size of the mesh and the failure mechanism observed in the etched mesh,

it is likely that even these scaffolds will not yield a good separator. To make something that could be tested, the most likely next step would be to cast a single thin layer of parylene (deposited onto an oil film to create a freestanding film), and then subsequently punctured mechanically to create the porosity needed for the separator.

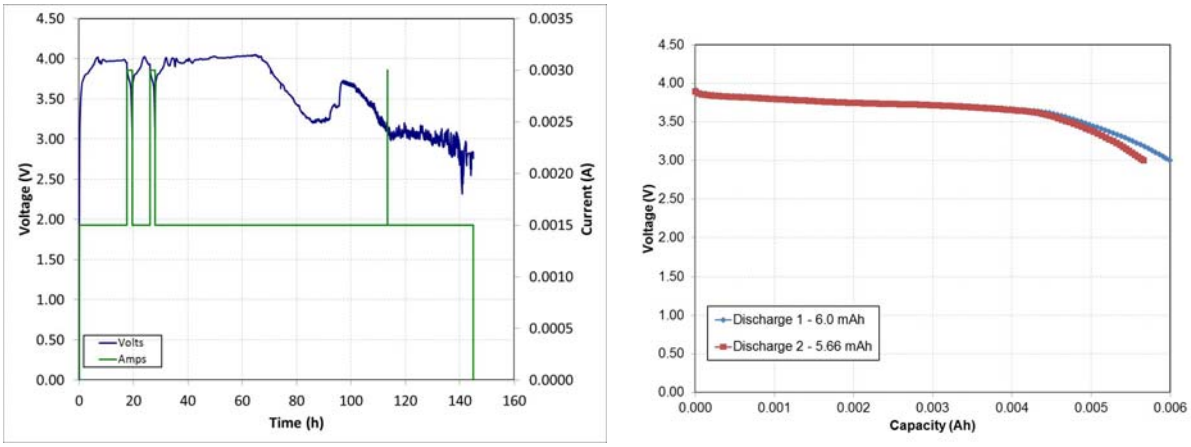

Figure 51. Formation cycle of with parylene coated bronze scaffold, with the scaffold etched away (left) and discharge capacity of the cell during the first two successful cycles (right).

3.6. Summary of Results

Poly(ester) separators for lithium-ion cells are an interesting alternative to conventional polyolefin-based materials. We have shown that under abuse conditions, localized cell heating and cell failures can occur at temperatures that correlate to the softening (~110 °C) or transition temperatures (135-160 °C) of conventional polyolefin separators. Separators based on PBT close the gap between separator phase transition and cell runaway temperatures and can improve the thermal stability of an entire cell or battery. We have shown that PBT separators can be prepared by electro-spinning PBT from solution into fiber mats and pressed into separator sheets. The resulting separators have good permeability and electrolyte wettability with conventional carbonate electrolytes. NMC/graphite cells made with PBT separators give comparable performance to commercial separators in terms of both capacity fade and rate capability with no observable chemical or electrochemical degradation. Impedance measurements of these PBT separators under conditions that mimic a battery environment show thermal stability to 210 °C, making these potentially much more abuse tolerant than polyolefin separators.

Methods for preparing a high temperature separator based upon a chemically resistant high temperature scaffold with a stabilizing binder were hindered by lack of an appropriate binder that was chemically resistant, soluble in solvents, and high temperature. Identification of a suitable high temperature polymer, poly-p-xylylene (parylene), showed that this polymer has promise as a separator, in that it is high temperature, easily deposited, and chemically stable at the anode and cathode potentials. However, creating a structure in the parylene that is porous to the

electrolyte proved problematic. Scaffolds of bronze, steel, ceramic, and etched bronze were tried, with no separator producing good results in battery performance, although, in the case of the etched bronze, this was likely not an issue with the material itself, but rather with the structure of the porosity introduced into the separator during processing.

4. CONCLUSIONS

As the application space for lithium-ion batteries continues to grow, the drive toward higher energy density batteries continues to advance. As these battery systems grow in physical size and in storage capacity, safety will continue to be critical to their success. In order to ensure safety for these systems, inherent safety and reliability at the cell level must be realized for normal use and off-normal conditions. Moreover, testing techniques to evaluate safety and reliability of these cells, batteries, and systems need to be advanced to meet the challenges associated with these technologies.

Electrolyte solvent choices for electrolytes can be made to reduce and may even eliminate electrolyte flammability with only minor tradeoffs in electrochemical performance. Electrolyte flammability during cell venting can be measured using robust and reliable testing technique. Reevaluation and modification of autoignition measurements for fuels can be made applicable to lithium-ion electrolyte under relevant test conditions in an effort to better understand the fundamental ignition characteristics of these complex solutions. Separator materials choices can be made in order to improve the thermal stability of those materials to close the gap between the separator phase transitions/softening temperatures and known thermal runaway temperatures for advanced lithium-ion battery cathodes. Advanced separators can be achieved through a number of processing techniques that are proven to be scalable, cost competitive, and widely applicable to manufacturing processes.

5. REFERENCES

1. http://hybridcars.com/news/battery-lab-explosion-rocks-gm-tech-center-44282.html
2. Hui Yang a, Guorong V. Zhuang b, Philip N. Ross Jr. b,∗Thermal stability of LiPF6 salt and Li-ion battery electrolytes containing LiPF6 Journal of Power Sources 161 (2006) 573–579
3. C. L. Campion, W. Li and B. L. Lucht, Thermal Decomposition of LiPF6-Based Electrolytes for Lithium-Ion Batteries, J. Electrochem. Soc. 2005 Vol 152(12) A2327-A2334
4. E.Zinigrad, L. Larugh-Asraf, J. S. Gnanaraj, M. Sprecher and D. Aurbach, Thermal stability of LiPF6, Thermochimica Acta 2005 Vol 43, 184-191
5. K. Xu, Review on Nonaqueous Liquid Electrolytes for Lithium-Based Rechargeable Batteries, Chemical Reviews, 104 (2004) 4303
6. J. T. Dudley, D. P. Wilkinson, G. Thomas, R. LeVae, S. Woo, H. Blom, C. Horvath, M. W. Juzkow, B. Denis, P. Juric, P. Aghakian and J. R. Dahn, Conductivity of electrolytes for rechargeable lithium batteries, Journal of Power Sources, 35 (1991) 59-82
7. D. Linden, T. B. Reddy (Eds.), *Handbook of Batteries*, 3rd ed., McGraw-Hill, New York, USA, 2002, Ch. 7.3.1.
8. T. Abe, N. Kawabata, Y. Mizutani, M. Inaba, and Z. Ogumi, Correlation Between Co-intercalation of Solvents and Electrochemical Intercalation of Lithium into Graphite in Propylene Carbonate Solution, J. Electrochem. Soc. 2003 150(3): A257-A261
9. P. Arora, Z. Zhang, *Chem. Rev*. **2004**, *104*, 4419
10. S. S. Zhang, *J. Power Sources* **2007**, *164*, 351.
11. D. Linden, T. B. Reddy (Eds.), *Handbook of Batteries*, 3rd ed., McGraw-Hill, New York, USA, 2002, pp. 23.31, 29.1-29.7.
12. P.P. Prosini, P. Villano, M. Carewska, Electrochim. Acta **48**, 227 (2002).
13. K.M. Kim, N.G. Park, K.S. Ryu, S.H. Chang, Electrochem. Acta **51**, 5636 (2006).
14. S.S. Zhang, K. Xu, T.R. Jow, J. Solid State Electrochem. **7**, 492 (2003).
15. H. –S. Jeong, D. -W. Kim, Y. U. Jeong, S. -Y. Lee, J. Power Sources **195**, 6116 (2010).
16. T. -H. Cho, M. Tanaka, H. Ohnishi, Y. Kondo, M. Yoshikazu, T. Nakamura, T. Sakai, J. Power Sources **195**, 4272 (2010).
17. P. G. Bruce, B. Scrosati, J. –M. Tarascon, Angew. Ch. Int. Ed. **47**, 2930 (2008).
18. T. H. Cho, M. Tanaka, H. Ohnish, Y. Kondo, M. Yoshkazu, T. Nakamura and T. Sakai, J. Power Sources **195**, 4272 (2010).
19. S. Augustin,V.D. Hennige, G. Horpel, C. Hying, Desalination **146**, 23 (2002).
20. V. Hennige, C. Hying, G. Horpel, P. Novak, J. Vetter, U.S. Patent Appl. 20,060,078,791 (2006).
21. E. P. Roth, D. H. Doughty, D. L. Pile, J. Power Sources **174**, 579 (2007).

22. S. S. Zhang, J. Power Sources, 162, 1379 (2006).
23. E.P. Roth, Society of Automotive Engineers, SAE 2008-01-0400 (2008).
24. E.G. Shim, T.H. Nam, J.G. Kim, H.S. Kim, S.I. Moon, J Power Sources, 172 (2007) 919-924.
25. T.H. Nam, E.G. Shim, J.G. Kim, H.S. Kim, S.I. Moon, J Electrochem Soc, 154 (2007) A957-A963.
26. H.F. Xiang, H.Y. Xu, Z.Z. Wang, C.H. Chen, Journal of Power Sources, 173 (2007) 562-564.
27. J.K. Feng, X.P. Ai, Y.L. Cao, H.X. Yang, Journal of Power Sources, 177 (2008) 194-198.
28. B. Dixon, MRS Bulletin, 30 (2005) 161-164.
29. D.H. Doughty, E.P. Roth, C.C. Crafts, G. Nagasubramanian, G. Henriksen, K. Amine, J Power Sources, 146 (2005) 116-120.
30. B.K. Mandal, A.K. Padhi, Z. Shi, S. Chakraborty, R. Filler, J Power Sources, 161 (2006) 1341-1345.
31. S.T. Fei, H.R. Allcock, J Power Sources, 195 (2010) 2082-2088.
32. J.L. Hu, Z.X. Jin, H. Hong, H. Zhan, Y.H. Zhou, Z.Y. Li, J Power Sources, 197 (2012) 297-300.
33. Y.E. Hyung, D.R. Vissers, K. Amine, J Power Sources, 119 (2003) 383-387.
34. X.M. Wang, E. Yasukawa, S. Kasuya, J Electrochem Soc, 148 (2001) A1058-A1065.
35. H. Ota, A. Kominato, W.J. Chun, E. Yasukawa, S. Kasuya, J Power Sources, 119 (2003) 393-398.
36. E.G. Shim, T.H. Nam, J.G. Kim, H.S. Kim, S.I. Moon, Electrochim Acta, 54 (2009) 2276-2283.
37. Y.J. Li, H. Zhan, L. Wu, Z.Y. Li, Y.H. Zhou, Solid State Ionics, 177 (2006) 1179-1183.
38. S.S. Zhang, K. Xu, T.R. Jow, Electrochem Solid St, 5 (2002) A206-A208.
39. S.S. Zhang, K. Xu, T.R. Jow, J Power Sources, 113 (2003) 166-172.
40. N.D. Nam, I.J. Park, J.G. Kim, Met Mater Int, 18 (2012) 189-196.
41. H.Y. Xu, S. Xie, Q.Y. Wang, X.L. Yao, Q.S. Wang, C.H. Chen, Electrochim Acta, 52 (2006) 636-642.
42. Lithium-Ion Batteries: Science and Technology, edited by M. Yoshio, R.J. Brodd, A. Kozawa (Springer-Verlag New York, LLC, 278-289, 2009).
43. S.T. Fei, H.R. Allcock, Mater. Res. Soc. Symp. Proc., 1127 (2009) 1127-T1101-1105.
44. T. Tsujikawa, K. Yabuta, T. Matsushita, T. Matsushima, K. Hayashi, M. Arakawa, J Power Sources, 189 (2009) 429-434.
45. C.W. Lee, R. Venkatachalapathy, J. Prakash, Electrochem Solid St, 3 (2000) 63-65.
46. J. Prakash, C.W. Lee, K. Amine, U.S. Patent, No. 6,455,200 (2002).
47. S. Izquierdo-Gonzales, W.T. Li, B.L. Lucht, J Power Sources, 135 (2004) 291-296.
48. S. Dalavi, M.Q. Xu, B. Ravdel, L. Zhou, B.L. Lucht, J Electrochem Soc, 157 (2010) A1113-A1120.
49. S.J. Harris, A. Timmons, W.J. Pitz, J Power Sources, 193 (2009) 855-858.
50. D. O'Hagan, Chem Soc Rev, 37 (2008) 308-319..
51. *CRC Handbook of Chemistry and Physics*, 79th ed., edited by D. R. Lide (CRC, Boca Raton, 1998–1999).
52. K. Xu, S.S. Zhang, J.L. Allen, T.R. Jow, J Electrochem Soc, 149 (2002) A1079-A1082.
53. M. Smart, K.A. Smith, R.V. Bugga, F.C. Krause, U.S. Patent 2010/0047695 A1, 2010.

54. J. Arai, J Appl Electrochem, 32 (2002) 1071-1079.
55. J. Arai, J Electrochem Soc, 150 (2003) A219-A228.
56. M. Morita, T. Kawasaki, N. Yoshimoto, M. Ishikawa, Electrochemistry, 71 (2003) 1067-1069.
57. K. Naoi, E. Iwama, Y. Honda, F. Shimodate, J Electrochem Soc, 157 (2010) A190-A195.
58. G. Nagasubramanian, C. Orendorff, J Power Sources, 196 (2011) 8604-8609.
59. G.T. Kim, S.S. Jeong, M. Joost, E. Rocca, M. Winter, S. Passerini, A. Balducci, J Power Sources, 196 (2011) 2187-2194.
60. A. Lewandowski, A. Swiderska-Mocek, J Power Sources, 194 (2009) 601-609.
61. S.F. Lux, M. Schmuck, S. Jeong, S. Passerini, M. Winter, A. Balducci, Int J Energ Res, 34 (2010) 97-106.
62. H. Nakagawa, S. Izuchi, K. Kuwana, T. Nukuda, Y. Aihara, J Electrochem Soc, 150 (2003) A695-A700.
63. J.K. Feng, Y.L. Cao, X.P. Ai, H.X. Yang, Electrochim Acta, 53 (2008) 8265-8268.
64. S. Werner, M. Haumann, P. Wasserscheid, Annu Rev Chem Biomol Eng, 1 (2010) 203-230.
65. S.Y. Chen, Z.X. Wang, H.L. Zhao, H.W. Qiao, H.L. Luan, L.Q. Chen, J Power Sources, 187 (2009) 229-232.
66. G. Nagasubramanian, Int J Electrochem Sc, 2 (2007) 913-922.
67. "Summary of ignition properties of jet fuels and other aircraft combustible fluids," TECHNICAL REPORT APAPL-TR-75-70, U.S. Bureau of Mines, Sept. 1975.
68. F. Buda, R. Bounaceur, V. Warth, P.A. Glaude, R. Fournet, F. Battin-Leclerc, Combust. Flame 142 (2005) 170–186; mechanism provided by F. Battin-Leclerc.
69. E. P. Roth, D. H. Doughty, J. Power Sources **128**, 308 (2004).
70. M. –K. Song, Y. –T. Kim, J. –Y. Cho, B. W. Cho, B. N. Popov, H. –W. Rhee, J. Power Sources 2004, 125, 10.
71. T. –H. Cho, M. Tanaka, H. Ohnishi, Y. Kondo, M. Yoshikazu, T. Nakamura, T. Sakai, J. Power Sources 2010, 195, 4272.
72. W. Yi, Z. Huaiyu, H. Jian, L. Yun, Z. Shushu, J. Power Sources 2009, 189, 616.
73. P. Kritzer, J. Power Sources 2006, 161, 1335.
74. D. T. Wong, S. A. Mullin, V. S. Battaglia, N. P. Balsara, J. Mem. Sci. 2012, 394-395, 175-183.
75. J. Jang and J. Won, Polymer 1998, 38, 4335.
76. T. Aoyama, A. J. Carlos, H. Saito, T. Inoue, Y. Niitsu, Polymer 1999, 40, 3657
77. D. Lin-Vein, N. B. Colthup, W. G. Fateley, J .G. Grasselli, The Handbook of Infrared and Raman Characteristic Frequencies of Organic Moledules, Academic Press, New York 1991.
78. R. S. Baldwin, W. R. Bennet, E. K. Wong, M. R. Lewton, M. K. Harris, Battery Separator Characterization and Evaluation Procedures for NASA's Advanced Lithium-Ion Batteries, NASA/TM-2010-216099, 2010.

DISTRIBUTION

1	MS0359	D. Chavez, LDRD Office	1911
1	MS0614	Thomas F. Wunsch	2546
1	MS0614	Christopher A. Apblett	2546
1	MS0614	William A. Averill	2546
1	MS0614	Kyle R. Fenton	2546
1	MS0614	Joshua Lamb	2546
1	MS0614	Ganesan Nagasubramanian	2546
1	MS0614	Christopher Orendorff	2546
1	MS0614	Leigh Anna Steele	2546
1	MS0734	Timothy N. Lambert	6124
1	MS9052	Christopher R. Shaddix	8367
1	MS9052	Manfred Geier	8367
1	MS0899	Technical Library	9536 (electronic copy)


Sandia National Laboratories